Friedrich-Alexander-Universität
Faculty of Sciences

Master's Thesis
in Physics

XMM-Newton Comparative X-ray Analysis of Galactic Supernova Remnants

Greesha Kapote

Supervisor:
Prof. Dr. Manami Sasaki
Dr. Karl Remeis Sternwarte, Astronomical Institute
Friedrich-Alexander-Universität Erlangen-Nürnberg

Submission date: March 13, 2026

Abstract

Supernova Remnants (SNRs) are excellent astrophysical laboratories for studying the energetic processes attributed with it like Supernova explosions, shock heating and the chemical enrichment of the interstellar medium. In this thesis, we provide a detailed spectral study of the three Galactic supernova remnants: G272.2 -3.2, G306.3 -0.9 and G299.2 -2.9 using archival data from the XMM-Newton X-ray Database. The imaging and spectral analysis investigates the ionization conditions, elemental abundances and sizes of the remnants in the X-ray regime.

The X-ray spectra and images were extracted from the data collected by the European Photon Imaging Camera (EPIC) instruments onboard the XMM-Newton satellite. The data was processed using the XMM-ESAS tasks and guidelines. The fitting of the data was done using the XSPEC application. The spectral analysis of all the three SNRs using the VNEI plasma models reveal that they have not yet reached an ionization equilibrium. The SNR G306.3 -0.9 also involves a cold component fitted using an APEC model. Another common component among the three SNRs was the Fe-L line at ~ 1.23 keV. Other parameters in the model have also been studied which give us a better understanding of these SNRs.

The imaging gives us a good glimpse of the X-ray morphology of the three remnants, with the SNR G272.2 -3.2 being a centrally-filled bright SNR. The SNR G306.3 -0.9 is also a asymmetric circular SNR but with a brightened semi-circle in the southern regions. Lastly, the SNR G299.2 -2.9 is a clear asymmetric shell-type SNR. Spectral analysis suggest a Type Ia characteristics for SNR G299.2 -2.9 and a Ca-rich transient SNR G306.3 -0.9. The analysis of G272.2 -3.2 does not show Fe abundances in its ejecta though previous researches conclude otherwise. The discussion section in the end describes all the spectral analysis results and compares them with other literature for each of the SNRs separately and also with eachother.

Contents

1 Introduction **2**

2 Interstellar Medium and Supernovae **5**
2.1 Interstellar Medium 5
2.2 Supernovae 7
2.2.1 Thermonuclear Supernovae 7
2.2.2 Core-Collapse Supernovae 8

3 Supernova Remnants **12**
3.1 Classification of SNRs 12
3.2 Evolution Phases of SNRs 14
3.3 Galactic SNRs 15

4 X-rays **18**
4.1 Emissions 18
4.1.1 Thermal Emissions 19
4.1.2 Non-Thermal Emissions 20
4.2 Detection 22
4.2.1 Imaging optics 22
4.2.2 X-ray Detectors 24

5 X-ray Data Analysis **27**
5.1 XMM-Newton 27
5.1.1 The Satellite 27
5.1.2 The Telescope 27
5.1.3 EPIC 30
5.1.4 Data Observation 31
5.1.5 Background 32
5.2 Data reduction and processing 32
5.3 Image Analysis 37
5.4 Spectral Analysis 41
5.4.1 Background Modeling 41
5.4.2 Source Modeling 44
5.5 Size Estimations 48

6 Discussion **51**
6.1 SNR G272.2 -3.2 51
6.2 SNR G306.3 -0.9 52
6.3 SNR G299.2 -2.9 52
6.4 Comparisons of the three SNRs 53

7 Conclusion **55**

Chapter 1

Introduction

The vast universe that we have known so far is said to be made of three types of substances i.e.'normal' matter, dark matter and dark energy. The normal matter which makes the visible universe including stars, planets, dust, gas and galaxies makes up only 5% of the universe. The rest 70% is said to be dark energy and 25% dark matter. Light (photons) emitted from many highly energetic astrophysical events such as the big bang, death of massive stars and gamma ray bursts to name a few, acts as an agent that brings us information about the dynamics of the universe. Supernovas and Supernova Remnants (SNRs) are such events that open up a treasure chest of information for observational astrophysicists about the life-cycle of stars and the evolution dynamics of galaxies. Supernovae are formed by a massive star explosive or a thermonuclear disruption of a white dwarf which inject huge amounts of energy, momentum and chemically rich material into the interstellar medium (ISM). This results in heating, compressing or ionization of gas surrounding it which in turn triggers more star formation. Supernova remnants emit photons in the whole range of the electromagnetic spectrum i.e. from radio synchrotron rays from relativistic electrons to optical light from shock heated filaments to X-ray and gamma radiation from very hot plasma and different particle acceleration processes. They provide the perfect environment for studying collisionless shocks and particle accelerations under physical conditions that are otherwise not attainable on terrestrially.

In this thesis we focus on the Galactic supernova remnants i.e. the SNRs that lie inside our galaxy, the Milky Way. Galactic supernova remnants provide more valuable research compared to the extragalactic ones in the sense that their proximity allows for higher spatial resolution and lets us perform detailed spectral analysis. Since supernovae are a primary source of heavy elements like oxygen, silicon and iron, the analysis of their elemental abundances provides us with an understanding of galactic chemical evolution and the origins of elements necessary for the formation of planet system and life. They also allow for multi-wavelength observations.

We take three different SNRs (G272.2 -3.2, G306.3 -0.9 and G299.2 -2.9) that lie within our galaxy and attempt to make a comparative study between them. We chose specifically these three SNRs because they provide a diverse array of characteristics which are evident in the results of our spectral analyses. First, we will review all the important information and concepts required to fully understand about what we are studying in chapters 2, 3 and 4. The next chapter comprises of

sections describing the XMM-Newton satellite (chp.5) with which the SNRs were observed, the pipeline of ESAS tasks used to reduce and process these data sets and then finally the image and spectral analysis. the spectral analysis includes the background and source modeling. This lets us study the physics of the objects which is discussed in chapter 6. The results of the spectral analyses of the individual SNRs have been compared to other researches done in the past. We also include a comparative study between the three different supernova remnants. The final conclusions are stated in chapter7 in the end.

Chapter 2

Interstellar Medium and Supernovae

2.1 Interstellar Medium

The Interstellar medium (ISM) is the most important component of any galaxy. We say this because it is where the stars are formed. It is also the space into which the stellar material is redeposited once the star dies. Most of the mass of a galaxy is said to be contained by dark matter while a small fraction of 10% is made of baryonic (protons and neutrons). In the early times, most of the baryonic (protons, neutrons) mass was in the gas of the interstellar medium. As galaxies evolve with time, this mass is then converted into stars or ejected from the ISM as galactic winds or just plundered into the intergalactic medium. We define the interstellar medium as everything that lies between the stars in a galaxy. This 'everything' consists of gas, dust (solid particles with sizes $\lesssim 1\,\mu$)m, cosmic rays, gravitational field, electromagnetic radiation field, magnetic field and the dark matter particles (Draine (2011)).

Most of the gas and dust in a spiral galaxy, for example the Milky Way, is concentrated within a thin gas disk. Within a radius of 15 kpc, the total mass of the Milky Way is around $\sim 10^{10} M_{\odot}$ (Kalberla and Kerp (2009)) of which the disk consists of a few $\sim (\times 10^{9}) M_{\odot}$. The rest is in the stars and dark matter. The interstellar gas is composed of around 70% hydrogen (H), 28% helium (He) and the other 2% are the other elements (Klessen and Glover (2016)). Of the total hydrogen, about 60% is in the form of H atoms, $\sim$ 20% in H_2 molecules and other $\sim$ 20% as ionized hydrogen. Hydrogen dominates here as it was formed during primordial nucleosynthesis shortly after the Big Bang. The ISM also includes heavy elements like C, O, Mg, Si and Fe enriched by stellar explosions, with the concentration declining along the radius of the disk away from the Galactic center. The dust component makes up only 1% of the ISM mass. It includes silicates, carbon- compounds and crystallized ammonia (NH_3), water (H_2O) and methane (CH_3). Dust usually absorbs and scatters blue light causing interstellar reddening. The ISM is a non-uniform and dynamic entity. It exists in thermodynamic phases which can be distinguished by density, temperature and ionization states. McKee and Ostriker (1977) added a third phase (Hot) to an already existing two-phase (Warm and Cold) model of the ISM given by Field et al. (1969). These phases are stated below:

*Coronal gas/ Hot Ionized Medium (**HIM**)*: This type of gas has been shock-heated to temperatures $\gtrsim 10^{5.5}$ K by blastwaves moving outward from supernova explosions. It is collisionally ionized and most of this type of gas has low density accounting for almost half of the Galactic disk volume and spans ~ 20 pc. Much of this gas expands above and below the disk, hence the region is termed as Hot Ionized Medium (HIM). It cools down by going through the processes of adiabatic expansion and X-ray emission. It can be observed through UV/ X-ray and radio synchrotron emissions.

*H II gas/ Warm Ionized Medium (**WIM**)*: This refers to the gas that has been photoionized by ultraviolet photons from hot massive O-type stars. This photoionized gas can also be from dense material from a nearby cloud in which case, the gas is called as an H I region. This type of gas can be studied from its optical line emissions and the thermal radio continuum.

*Warm H I/ Warm Neutral Medium (**WNM**)*: This phase of atomic gas is heated to temperatures of $\sim 10^{3.7}$ K by photoelectrons coming from the dust in the local ISM. The gas has densities $n_H \sim 0.6\,cm^{-3}$ and fills up a significant volume of the disk ($\sim 40\%$). This gas can be studied from the H I 21-cm emission or absorption. It can also be studied from its optical/ UV emission.

*Cool H I/ Cold Neutral Medium (**CNM**)*: It consists of atomic gas at temperatures of $\sim 10^2$ K with density $n_H \sim 30\,cm^{-3}$ which fills $\sim 1\%$ of the local ISM. Similar to the previous phase, the H I 21-cm emission and optical/ UV absorption lines can be used to study this region.

Molecular Medium: This phase can be subdivided into two parts. One, the Diffuse molecular gas and second, the Dense molecular gas. The Dense gas ($n_H \gtrsim 10^3\,cm^{-3}$) contains clouds bound together by gravity. This also makes it the region where star formation occurs.
As stated earlier, the ISM is very dynamic. The baryonic particles are always undergoing phase transformations. These changes occur as ionizing photons from stars convert cold molecular gas to hot H II. Hot gas can be cooled down by the process of radiative cooling, atom formation occurs due to the recombination of ions and electrons and H_2 molecules form by recombining H atoms.

The Interstellar medium is very central to the stellar life cycle. Initially, Dense molecular clouds form in the ISM which then collapse due to their own gravity. A protostar emerges from this collapse. Then the process of nuclear fusion provides for the growth of the star. At the end of its life, the star dies explosively (supernova), sending shock waves into the ISM, hence returning or enriching the ISM with heavy elements and other materials which serve as the building blocks for the future generation of stars (2.1). This enriched elemental material changes the chemical composition of the ISM and subsequently the metallicity of the future stars.

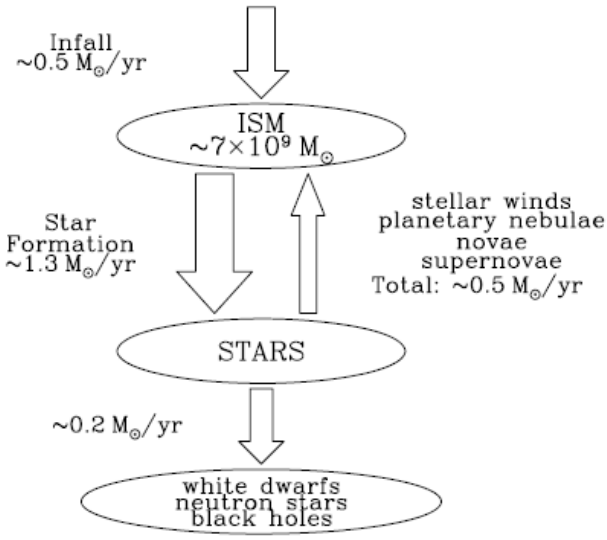

Figure 2.1: Flow of baryonic matter in the Milky Way galaxy (Draine (2011))

2.2 Supernovae

A Supernova is one of the most powerful and spectacular events occurring in the cosmos. They can outshine their entire galaxy for a few moments. Supernovae occur when a star reaches the end of its life and explodes violently sending shock waves into the surrounding space at ballistic speeds. These shock waves enrich the surrounding interstellar medium with heavy elements and influence galaxy and planet system formations.

The types of supernovae (SNe) can be broadly classified based on the explosion processes: core collapse SNe and thermonuclear SNe. Based on spectroscopy, Minkowski (1941) divided supernovae into two type (fig.2.2a): Type I that do not show hydrogen absorption in their spectra and Type II that do show it. The type I SNe can be core-collapse or thermonuclear types whereas Type II are essentially core-collapse type of supernovae. The Type I supernovae can be further sub-divided into Type Ia (thermonuclear SN with Si II absorption line), Type Ib (core-collapse SN with no Si II or He I lines) and Type Ic (core-collapse SN with He I but no Si II lines). Type II supernovae are also sub-classified based on their light curves (fig.2.2b). A plateau in the light curve of a supernova is classified as Type II-P while the one with a linear light curve is classified as a Type II-L. There also exists a Type II-b which show a weak H-line just after the explosion for a small amount of time. A fourth type is the Type II-n SN characterized by narrow emission lines in their spectra (Helder et al. (2012)).

2.2.1 Thermonuclear Supernovae

Thermonuclear or Type Ia supernovae occur in binary star systems which include atleast one white dwarf. A white dwarf is a compact object left behind when a star with an inital mass around $8M_{\odot}$ expels its outer layers due to exhaustion of its nuclear fuel. This leave behind a very dense core supported by electron degeneracy pressure to counter the gravitational pressure. The Type Ia SNe are

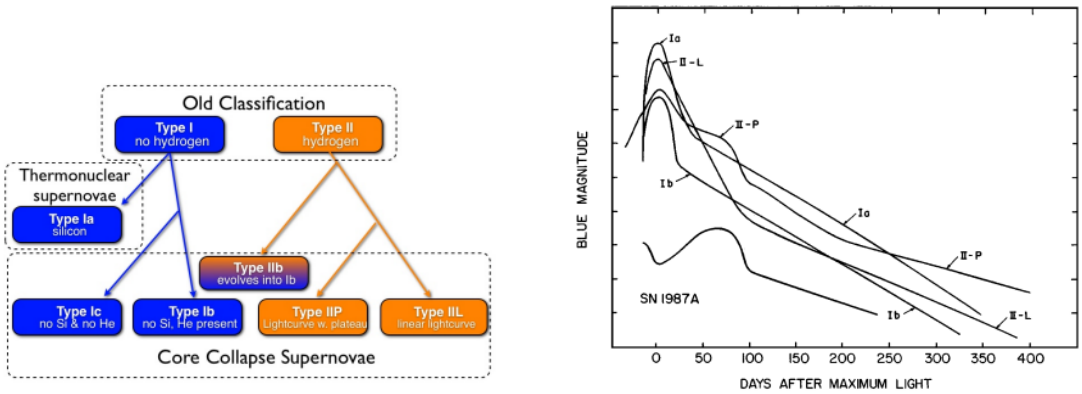

(a) (b)

Figure 2.2: (a) Classification of supernovae from optical spectroscopy and light curve analyses (Vink (2012)); (b) schematic of the light curves of Types Ia, Ib (includes Ic), II-L and II-P for comparison (Filippenko (1997))

called thermonuclear because, the explosion energy originates from explosive nuclear burning instead of gravitational collapse. Most of the Type Ia explosions show almost the same brightness levels except for a few minor variations. Hence, they also serve as *standard candles* for measuring cosmic distances. Their explosion mechanism follow that the white dwarf accretes matter from its companion star (either a main sequence star or a red giant) until it reaches the Chandrasekhar limit($1.38\,M_{\odot}$). In case of a second white dwarf companion, the two white dwarfs shrink their orbits due to gravitational radiation and ultimately merge into each other reaching a mass exceeding the Chandrasekhar limit. In both the scenarios, once this limit is reached, the carbon and oxygen in the star's core ignite under degenerate conditions, starting a thermonuclear runaway reaction. In this, the carbon nuclei fuse rapidly producing a drastic increase in energy and the temperature rises uncontrollably. The nuclear burning spreads through the star first as subsonic flames (Deflagration) or as a supersonic shock wave that compresses and heats the plasma (Detonation). These processes as a whole are termed as 'Delayed Detonation' model given by Khokhlov (1991). The star is completely burnt and disrupted at the of this explosion with no compact remnant left behind. The SN explosion synthesizes large amounts of heavy metals especially, iron (Fe), radioactive nickel (^{56}Ni) which breaks down through the $^{56}\mathrm{Ni} \rightarrow {}^{56}\mathrm{Co} \rightarrow {}^{56}\mathrm{Fe}$ channel. This decay chain produces gamma rays which gives the supernova's light curve a peak as shown in fig.2.2b. The spectral analysis of this type of SN also reveals the presence of other intermediate elements like Si, S, Ca and an absence of hydrogen lines.

2.2.2 Core-Collapse Supernovae

Core-Collapse (CC) supernovae occur at the end of the life of massive stars with masses $\gtrsim 8M_{\odot}$. Their progenitor stars contains different layers of elements starting from an iron core to silicon, magnesium, oxygen to an outermost hydrogen layer. The formation of the innermost iron layer marks the beginning of the death of the star as the core does not burn any further through fusion. The core then collapses

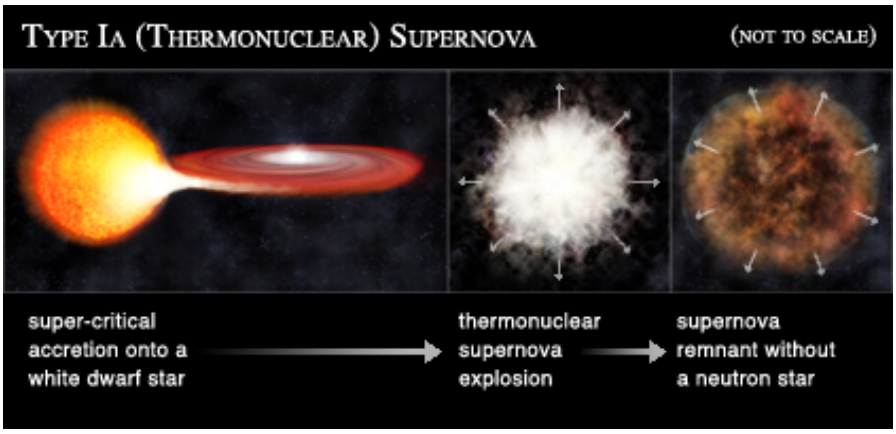

Figure 2.3: Illustration of the mechanism of a Type Ia (thermonuclear) supernova [Illustrator: NASA/CXC/M.Weiss]

either into a proto-neutron star or a black hole for the most mmassive stars. The energy ($\gtrsim 10^{53}$ erg) released in this collapse is mostly in the form of neutrinos. The collapse suddenly stops as the proto-neutron star is formed and steers a shock wave through the accreting material. The ejecta of the core-collapse SNe mainly contains materials (Si- and Fe- group elements) formed from the nucleosynthesis process. These elements are synthesized from protons and α-particles which were left behind after the heavy elements disintegrated in the extreme heat of the regions around the collapsing core. Some of the elements synthesized are also radioactive like ^{56}Ni and ^{44}Ti. The ^{56}Ni decays into ^{56}Co and then to ^{56}Fe producing immense amount of energy that heats up the ejecta.

Of all the core-collapse supernovae, the Types Ib and Ic supernovae originate from massive stars that are stripped off their hydrogen envelope before exploding. They seem to have lost their H-rich envelope due to stellar wind mass loss or through binary interactions. in case of Type Ic, the mass loss also causes removal of the He layer. The progenitors of Type Ib SNe are often Wolf-Rayet stars which are massive, extremely hot stars with strong stellar winds. Type Ic on the other hand have massive progenitors with a carbon-oxygen cores since their H and He layers have been stripped off. Of the Type II supernovae, the Type II-P has a plateau in its light curve which is caused by the recombination of the expanding hydrogen layer of the star. This recombination releases energy gradually. As opposed to this, the Type II-L SNe have a steadily declining slope in its light curve as their stars have lesser hydrogen envelope, hence, the energy escapes quickly. The Type II-n are characterized by narrow line emission spectra which are produced by the interaction of the circumstellar medium with the ejecta which was expelled by the progenitor star before exploding. The Type II-b is a transitional subtype between the Type II and Ib such that its spectrum initially shows hydrogen lines like a type II SN but is later helium dominated like a Type Ib SN. This is because its progenitor star retains only a thin layer of hydrogen mostly due to binary interactions.

Other subclasses of non-traditional supernovae have also been identified. Firstly, the Pair-Instability SNe which occur in extremely massive ($> 100 M_{\odot}$) stars. In this case, gamma radiation creates electron-positron pairs during the O-burning stage,

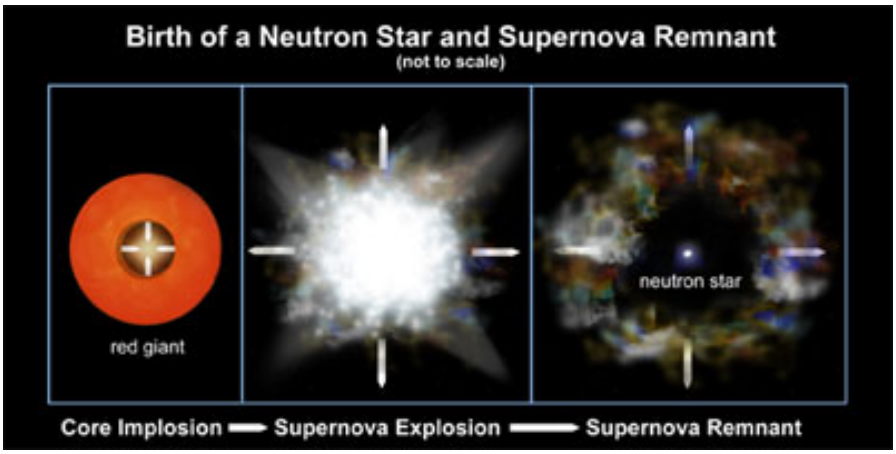

Figure 2.4: Illustration of the mechanism of a core-collapse supernova with a resultant neutron star [Illustrator: NASA/CXC/M.Weiss]

hence destabilizing the star and leading to an explosion such that the whole star is destroyed, leaving no remnant behind. There also exist Electron-capture SNe that occur in stars with $\sim 8 - 10\, M_{\odot}$. Their core never reaches the iron- burning stage and develop a degenerate O-Ne-Mg core. As the name suggests, atomic nuclei of these elements capture electrons. As the electron degeneracy pressure that sustains the star drops, the star collapses under gravity. The inner core then rebounds causing an explosion. These SNe usually also result into neutron stars.

Chapter 3

Supernova Remnants

We learned in the previous chapter that supernovae are the stellar explosions that occur at end of some star's life. These events occur either through core collapse of massive stars (type II, Ib, Ic) or through thermonuclear explosions of white dwarfs (type Ia). Supernova Remnants (SNRs) are the end-products of such explosive deaths of stars (Supernovae). The expelled materials from a supernova expand into the surrounding interstellar medium at extremely high speeds generating shock waves that can heat, ionize and compress the ISM gas. This results in structure formations in the ISM which are then called as Supernova Remnants (SNRs). The remnants play an important role in maintaining the galactic ecology. They redistribute heavy elements generated through nucleosynthesis, trigger star formation through shock compressions and aid Galactic cosmic ray acceleration by diffusive shock acceleration.

3.1 Classification of SNRs

One might intuitively deduce that the different types of supernova remnants are the same as the types of their supernovae. But the distinction here is not so direct and easy. The SNRs are therefore classified based on their morphology. This classification is given below (Vink (2012)).

Shell type SNRs: This type of SNR is created when the blast wave moves through the ISM making a shell of shock heated plasma. It is characterized by bright emission concentrated along the outer boundaries of a roughly circular or elliptical shell. The shock plasma predominately emits thermal X-rays. Shock fronts can be visible in optical wavelengths. There is also proof of cosmic ray accelerate at these shock boundaries. The shell type of SNRs usually originate from Type Ia Supernovae where the progenitor white dwarf lacks pre-explosion mass loss, hence producing relatively symmetric remnants. The common examples of this type SNR include Tycho's Supernova Remnant or the SN 1006 (fig.3.1).

Plerions: In case of a core collapse supernova, we may expect the presence of a neutron star, which loses energy at a certain rate producing relativistic electrons and positrons that run into a shock. These electrons/ positrons diffuse away from the shock creating a nebula of particles which emit synchrotron radiation ranging from radio to soft gamma-rays. Such SNRs are characterized by the lack of a prominent outer shell and instead have bright central synchrotron emission. They

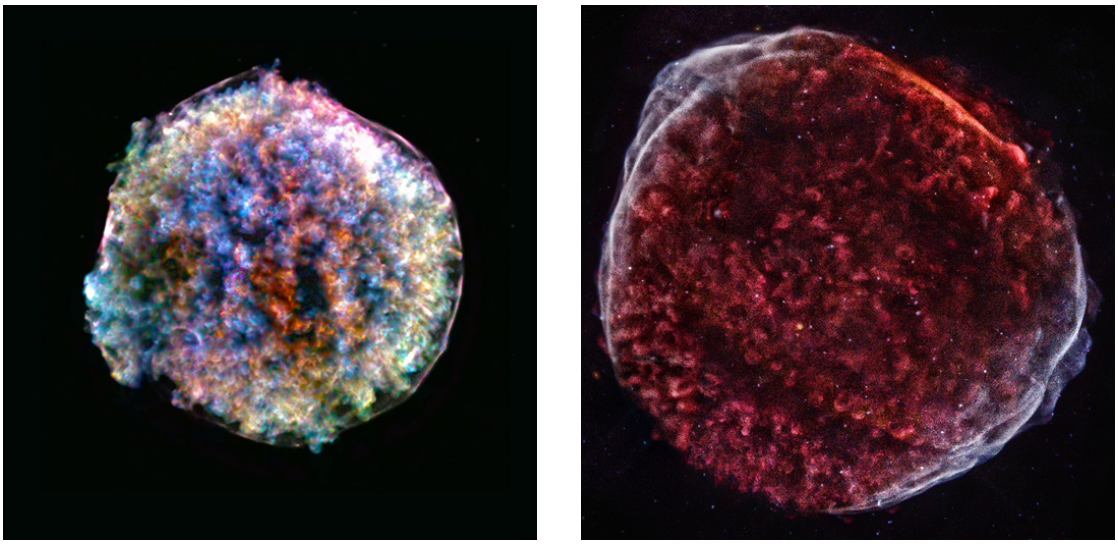

(a) (b)

Figure 3.1: Chandra X-ray images of shell type (a) Tycho's SNR and (b) SN 1006.[Image credits:(a)NASA/CXC/RIKEN and GSFC/T; (b) NASA/CXC/Middlebury College/F.Winkler (Winkler (2013))]

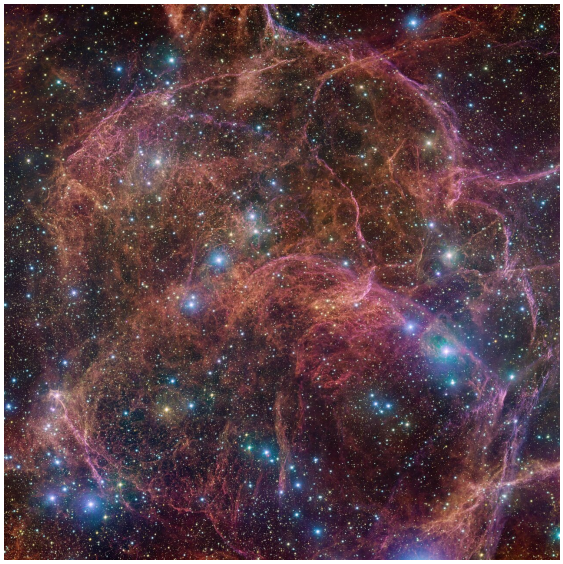

Figure 3.2: Image of Composite type Vela SNR showing the gaseous filaments, taken from the OmegaCAM camera at the VLT Survey Telescope (Paranal Observatory, ESO) .[Image credits:ESO/VPHAS + team]

have a flat radio spectral index and strong polarizations indicating magnetic fields.

Composite SNRs: These type of supernova remnants exhibit both shell type and plerionic SNR characteristics. Young energetic pulsars with ages $\lesssim$ 20000 yrs have blown a pulsar wind nebula while being surrounded by the shell of the SNR. The composite type of SNR can also be further classified into first, a Classical Composite with a clear shell and a central pulsar wind nebula and second, a Mixed-Morphology remnant with a radio shell and a centrally filled thermal X-ray emission. An example of such type is the famous Vela Supernova Remnant (fig.3.2).

3.2 Evolution Phases of SNRs

The evolution of Supernova Remnants is distributed into four phases as devised by Woltjer (1972) based on the hydrodynamic interactions of the ejecta from the supernova with the ambient interstellar medium.

Free Expansion Phase: When a star undergoes a supernova, the stellar ejecta expands into the ambient medium, creating a shock front called the *forward shock*. Their expansion velocities can be in the range of $\sim 5000 - 20000$ km/s (Chevalier (1982)). Here, the ISM mass is almost negligible in comparison to the mass of ejecta ($M_{medium} \ll M_{ejecta}$). Hence, the shock wave propagates almost 'freely'. As the forward shock sweeps up the ambient medium, it slows down, in reaction to which a second wave called the *reverse shock* is formed that heads in the opposite direction of the forward shock (fig.3.3). The outer shockfront grows roughly proportional to the age of the SNR as:

$$R(t) \propto t \tag{3.1}$$

The shocked plasma emits strong X-rays as the temperatures exceed $\sim 10^7 - 10^9$ K. This phase ends when $M_{medium} \approx M_{ejecta}$.

Sedov-Taylor (Adiabatic) Phase: After a few hundred years, most of the energy is transferred from the ejecta to the shock-heated shell. The radiative losses are still negligible in this phase, hence, the supernova remnant expands adiabatically. This phase usually lasts from $\sim$ 1000 to 20000 yrs as the expansion slows down. The phase follows the Sedov- Taylor self-similar solution (Sedov (1959); Taylor (1950)) which assumes the explosion energy (E $\sim 10^{151}$ erg) to be

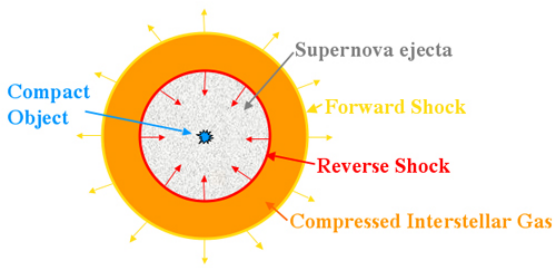

Figure 3.3: Schematic of forward and reverse shocks created when the shock wave interacts with the ambient medium. [Credits:Cosmos/Swinburne University]

instantaneously injected into the uniform ambient medium with density ρ. Also assuming no radiative losses, the shock radius evolves as:

$$R(t) \propto \left(\frac{Et^2}{\rho}\right)^{1/5} \tag{3.2}$$

Accordingly the expansion slows down with time (t) as,

$$v(t) \propto t^{-3/5} \tag{3.3}$$

This phase is characterized by a bright limb-brightened shell morphology with radio synchrotron shell- and strong thermal X-ray- emissions.

Pressure-driven Snowplow (Radiative) Phase: As the shock slows down, its temperature falls below $\sim 10^4$ K. The cooling time becomes shorter than the expansion time. This causes formation of a thin, dense shell with a got low-density interior maintaining pressure. The shocked gas radiates thermal energy in the form of line emissions of H, He, C, N and O (Raymond (1979)). The expansion of the shock then develops as:

$$R(t) \propto t^{2/7} \tag{3.4}$$

One can also observe enhanced optical line emissions of Hα, [O III] and [S II]. The cygnus loop is a good example of an SNR in this phase.

Momentum-Conserving Snowplow (Dissipation) Phase: In this phase, the shock has reached the point where the interior pressure loses its significance and the expansion is purely driven by momentum conservation.

$$R(t) \propto t^{1/4} \tag{3.5}$$

The shock velocity approaches the ISM turbulent velocity value i.e. $v \sim 10$ km/s. Hence, the remnant slowly loses its distinctive shell structure and merges with the ambient medium. This merging of boundaries contributes to the addition of turbulence, heavy elements and kinetic energy into the ISM.

The morphology of the above mentioned phases of an SNR depends heavily on the ambient medium density gradients, magnetic fields, progenitor wind bubbles and explosion asymmetry.

3.3 Galactic SNRs

We would now focus on the supernova remnants in our galaxy, the Milky Way. Currently, ∼300-400 SNRs (Ferrand and Safi-Harb (2012)) have been classified as Galactic SNRs though many estimates concede to the existence of atleast 1000 or more (Ranasinghe and Leahy (2022)) at any given time in radio. Many SNRs remain undetected due to dust obscuration or low surface brightness of the SNR. SNRs at higher latitudes also remain undetected as many surveys focus on the Galactic plane. X-ray observations are also very widely used for probing SNRs in the Galaxy (Leahy et al. (2020)). Green (2025) has most recently cataloged 310 confirmed Galactic SNR sources. It estimates a Galactic SNR rate of 2 to 3 per

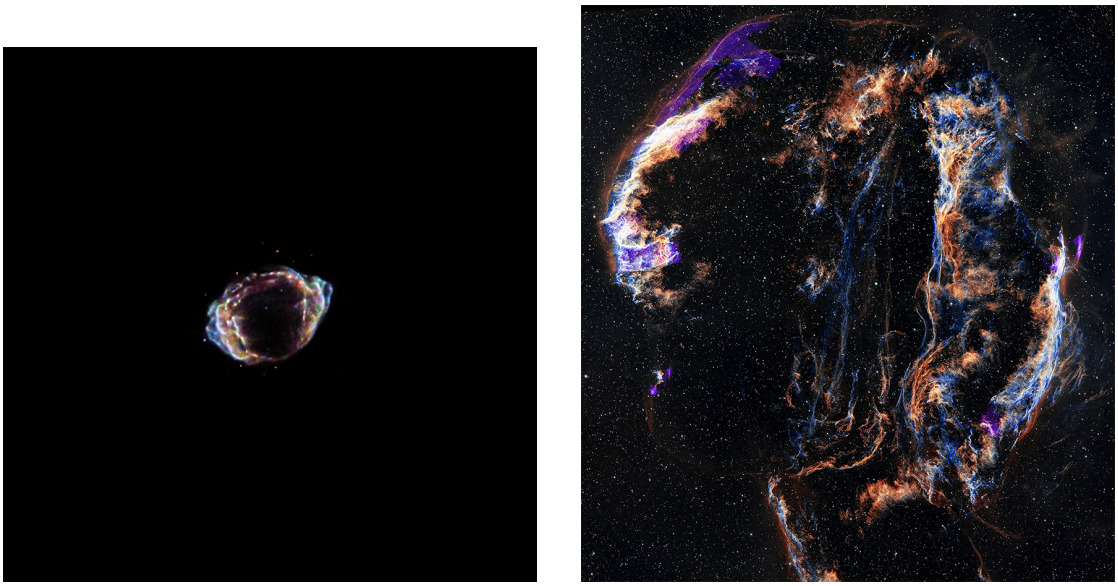

(a) (b)

Figure 3.4: Chandra images of SNRs (a)G1.9 +0.3 and (b) the Cygnus loop which are the smallest and one of the largest known Galactic SNRs respectively. [Image credits: (a)X-ray: NASA/CXC/NCSU/Borkowski et al. (2013) (b)X-ray: NASA/SAO/CXC; Optical: John Stone (Astrobin)]

century with an average observable lifetime of $\sim 10^5$ yrs. Most of the SNRs stated in the catalog are concentrated along the Galactic plane where most of the massive stars form (core-collapse type SN progenitors). Latitudinally, most of the SNR s are found around $|b| \lesssim 5°$. The few SNRs found at higher galactic latitudes are usually from runaway progenitor stars or SNR expanding into the low-density halo regions. Longitudinally, the distribution of SNRs is not so uniform. Most of the SNRs are concentrated towards the inner part of the Galaxy with distributions in the range of $l \approx 10° - 60°$. Radially, most SNRs are located within a few kilo-parsecs from the center of the Galactic disk with the maximum density at $\approx 4-6$ kpc. Their distribution is consistent with the molecular gas distribution in the spiral arms and the distribution of massive star formations. In the Milky Way galaxy, the sizes of the SNR range from < 5 arcmin for the young, distant remnants, $5 - 30$ arcmin for the middle-aged ones to the older-nearby remnants sized $> 1°$. The majority ($\sim 80\%$) of SNRs discovered are Shell-type SNRs while the plerions make up the least of the population. Many old and distant SNRs become hard to detect due to their low brightness and smaller size respectively. Many missions like, XMM-Newton, Chandra, Einstein Probe, eROSITA are used to study the Galactic SNRs in X-rays. Other missions in the radio energies include ASKAP (Australian Square Kilometer Array Pathfinder), MeerKAT used in conjunction of eROSITA, LOFAR (Low Frequency Array) and the VLA (Very Large Array) to name a few.

Chapter 4

X-rays

Within the electromagnetic spectrum, X-Rays are typically understood as radiation with energies ranging from about 100 eV to 100 keV. This corresponds to a wavelength range between 0.01 nm and 10 nm. Therefore, they lie between gamma rays and Ultraviolet radiation and are considered as high energy electromagnetic radiation. They have been first detected in the year 1895 by the German scientist Wilhelm C. Röntgen . During Experiments with a cathode ray tube, Röntgen was able to create X-rays and observed their ability of penetrating through solid Objects. We are now interested in studying the X-rays coming from cosmic sources to get a better picture of the universe. The Earth's atmosphere shields the incoming dangerous X-rays. Hence, they need to be detected extra-terrestrially. The first X-rays coming from the sun were detected in 1949 by a detector onboard a V-2 rocket. In 1962, the first X-ray cosmic source called Scorpius X-1 was discovered on an Aerobee rocket. In the following years, astronomers switched to balloons for observations which took the X-ray detectors to a height of almost 50km up from the ground. This offered them longer exposures to make their observations. The first satellite committed to X-ray astronomy was the Uhuru satellite (Jagoda et al. (1972)) launched in 1970 by NASA. It conducted an all-sky survey in the 2 - 20 keV X-ray band and identified 339 X-ray sources. Many other X-ray missions followed like the Ariel 5 (1974), SAS-3 (1975), HEAO-1 (1977) and EXOSAT (1983) to name a few. In the recent years, XMM-Newton (1999), Chandra (1999), eROSITA (2019), the Einstein Probe (2024), have carried out some of the best observations in X-rays so far. The NewATHENA (Advanced Telescope for High ENergy Astrophysics) mission by the ESA is scheduled to be launched in 2037 (Athena). It would be the largest X-ray observatory and aims to study the hot and energetic universe.

4.1 Emissions

Since we have established from the previous chapters that many astrophysical sources emit energies in the X-ray regime, we would now dwell into the details of the processes through which these radiations are created. The processes are broadly divided into two types based on the type of emissions: Thermal and Non-thermal emissions. Thermal emissions are produced from atomic collisions or interactions in a system under thermal equilibrium like in the hot plasmas in our case. Non-thermal emissions on the other hand are generated by high energy, non-

thermal particles like cosmic rays by acceleration or in the presence of a magnetic field.

4.1.1 Thermal Emissions

4.1.1.1 Blackbody Radiation

Blackbody radiation is the electromagnetic radiation that is emitted by an object that ideally absorbs all incident radiation and then re-emits the energy according to its temperature. It show absolutely zero reflectivity. The intensity of a blackbody radiation is given by Planck's law :

$$B(\nu, T) = \frac{2h\nu^3}{c^2} \frac{1}{e^{h\nu/kT} - 1} \tag{4.1}$$

where $B(\nu, T)$ is spectral radiance, h is the Planck's constant, ν is frequency, c is the speed of light, k is the Boltzmann constant and T is the absolute temperature of the blackbody. The spectrum of a blackbody shows a continuum with a single peak wavelength (λ_{max}) i.e. where the emission is maximum and is given by Wien's Displacement law:

$$\lambda_{max} T = 2.898 \times 10^{-3} mK \tag{4.2}$$

The radiation intensity increases and the peaks shift towards shorter wavelengths with increasing temperatures. Many astrophysical objects, like stars and accretion disks, emit this kind of radiation.

4.1.1.2 Bremsstrahlung Radiation

Thermal bremsstrahlung (German translation:'braking radiation') is the radiation produced when free electrons are accelerated (or decelerated) in the electric field generated by ions present in a hot plasma. Electrons move with large velocities due to the thermal energy in a hot ionized plasma. An electron is deflected by Coulomb force when it passes from near a positively charged ion. This deflection implies the electron is accelerated and hence emits electromagnetic radiation. The energy emitted by the photon is given as:

$$E = h\nu \tag{4.3}$$

This radiation is also termed as *free-free radiation* as the electron remains in free motion both before and after the interaction (fig.4.1). The electrons follow the Maxwell-Boltzmann velocity distribution:

$$f(v) \propto e^{-mv^2/2kT} \tag{4.4}$$

This equation shows the temperature dependence of the radiation spectrum. The radiation spectrum shows a continuum, as the electron may lose an unfixed amount of their kinetic energy, with an exponential cutoff at higher energies. This type of emission is very common in hot plasmas of temperature $\sim 10^7 - 10^8$ K in sources like supernova remnants (SNRs), hot interstellar medium and galaxy clusters when observed in X-rays.

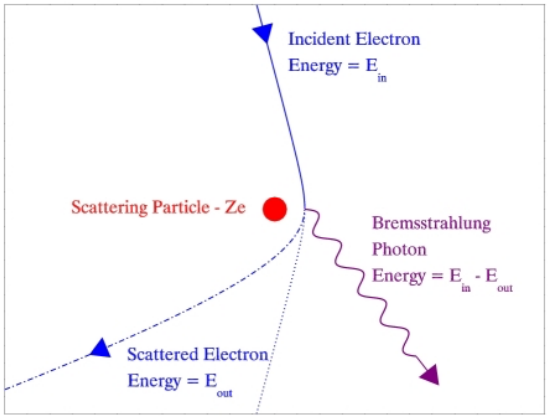

Figure 4.1: Diagram showing free-free interaction of an electron with an atom with charge Ze which releases bremsstrahlung [Credits:nasa/wiki]

4.1.1.3 Fluorescence line emission

Fluorescence emission is produced when high energy radiation is absorbed by an atom which leads some of its electron to move to lower energy states and emit photons in result. X-ray fluorescence occurs when the incident radiation specifically removes the inner-shell (usually K or L) electrons of an atom creating a vacancy (hole) which makes the atom unstable. Electrons from an outer shell transition to fill up these holes, producing photons with energies in the X-ray band (fig.4.2a). The emitted X-ray photons have discrete energies which is the energy difference between the shells they transitioned. In an SNR, high-energy X-rays are produced in the hot plasma through the process of bremsstrahlung as explained earlier. These X-rays then interact with the neutral or weakly-ionized material nearby causing X-ray fluorescence. the Fe Kα at 6.4 keV is one of the most prominent lines detected in the X-ray spectrum of an SNR. A strong Fe Kα also suggests the presence of cold dense material or molecular clouds near the SNR (Yamaguchi et al. (2014)). Detecting fluorescence lines also helps us identify the elements produced in the nucleosynthesis process in a supernova (fig.4.2b). Satellites like XMM-Newton and Chandra have helped astrophysicists perform high-resolution X-ray spectroscopy to study the ejecta from SNRs.

4.1.2 Non-Thermal Emissions

4.1.2.1 Synchrotron Radiation

Non-thermal synchrotron emissions in SNRs are produced from electrons accelerated to relativistic energies at the forward shocks and in central pulsar powered wind nebulae. These electrons accelerated in the SNR follow a helical motion governed by the Lorentz force acting on it in the magnetic fields ($\sim 10 - 100\,\mu$G):

$$F = q(\mathbf{v} \times \mathbf{B}) \tag{4.5}$$

This results in the emission of high energy X-ray photons (fig.4.3a). The characteristic synchrotron frequency is give by:

$$\nu \approx \frac{3}{2}\gamma^2 \frac{eB}{2\pi m_e c} \tag{4.6}$$

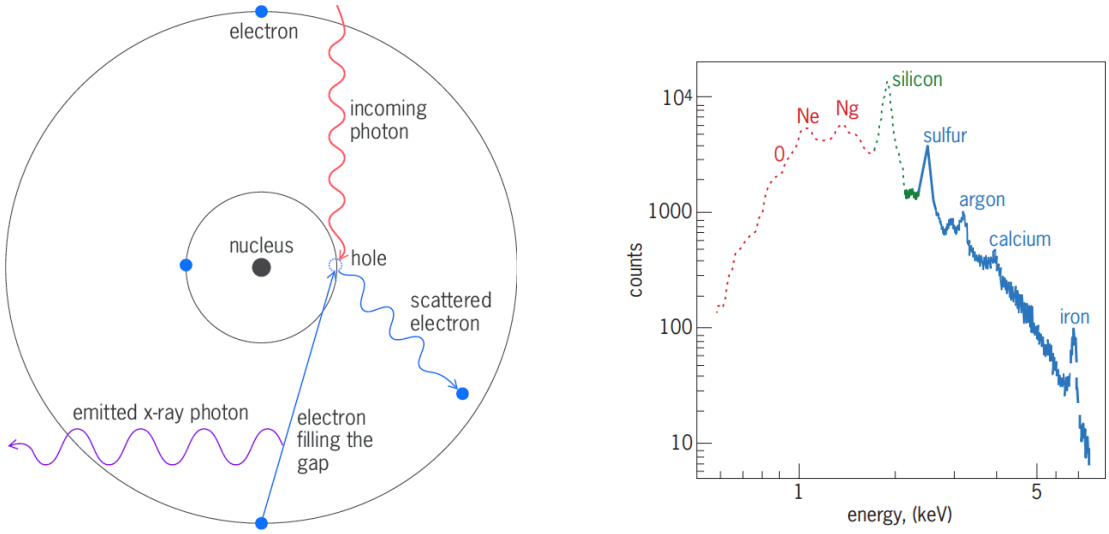

(a) (b)

Figure 4.2: (a) Diagram of X-ray fluorescence line emission ;(b) Chandra spectrum of Cassiopeia A illustrating characteristic X-ray emission line peaks of different elements [Credits:(a) and (b) McLaughlin (2013)]

where γ is the Lorentz factor of the electron, B is the strength of the magnetic field, e and m_e is the electron charge and mass and c is the speed of light. The radiation generates a powerlaw spectrum. The detection of synchrotron emissions provides an evidence for the cosmic ray acceleration (to TeV energies) by SNR shocks.

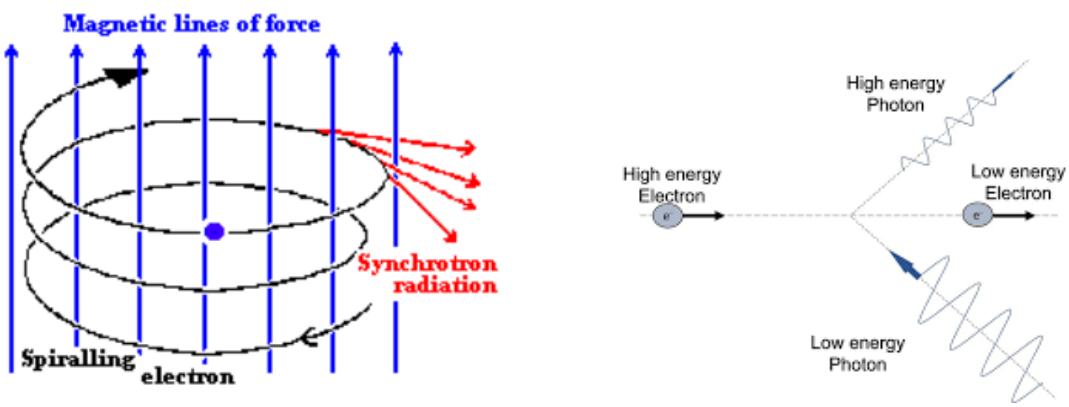

(a) (b)

Figure 4.3: Diagrammatic representation of the production of (a) Synchrotron radiation [credits: heasarc/nasa] and (b) Inverse Compton scattering (Tracz (2022))

4.1.2.2 Inverse Compton Scattering

As opposed to normal Compton scattering, low-energy photons are boosted into higher-energy photons through interaction with relativistic electrons which were produced by shock waves in an SNR (fig.4.3b). The low-energy photons required for this process usually come from either the Cosmic Microwave Background

(CMB) which is omnipresent in the space or infrared radiation produced by interstellar dust or heated circumstellar material. The energy gained by the photons is given by:

$$E_\gamma \approx \gamma^2 E_{ph} \tag{4.7}$$

where E_{ph} is the energy of the initial photon and γ is the Lorentz factor of the electron. The output photons have energies in the range of $\sim$ GeV- TeV.

4.2 Detection

The next step in the study of X-rays after identifying their generation processes is to know how to find them. This can be done by using telescopes with focusing optics and detectors as described below.

4.2.1 Imaging optics

Imaging is one of the most important methods used for studying supernova remnants. Imaging usually helps reveal the structure of shock fronts, ejecta distribution and morphology of the SNR. The focusing optics used for X-ray imaging is not the same as those used for visible light. This is because, unlike visible light, X-rays incident on a material usually penetrate or get absorbed depending on the thickness of the material. they follow the process of *total external reflection.* A solid medium here is described by a (complex) refractive index :

$$n = 1 - \delta + i\beta \tag{4.8}$$

where δ and β are optical constants that have a very small value in the X-ray regime. They depend on wavelength and the atomic scattering factor. For a conductive medium, $\beta \neq 0$ causing the refracted X-ray to decay exponentially due to absorption. X-rays generally use *grazing incidence* optics where as the name suggests, the X-rays are incident on the material surface at small grazing angles such that the X-rays can reflect off it (fig.4.4). The incident and refracted rays follow Snell's law. Using grazing incident angle ($\theta = \pi/2 - \phi$) measured relative to the tangent of the surface, the Snell's law is transforms into:

$$cos\,\theta_r = cos\,\theta_i/(1-\delta) \tag{4.9}$$

where θ_r and θ_i are the refracted and incident angles respectively. Since $\delta > 0$ for X-rays, there exists a *critical grazing angle* (θ_c) below which total external reflection occurs. For small angles:

$$\theta_c \approx \sqrt{2\delta} \tag{4.10}$$

At X-ray energies, the optical constant (δ) depends on photon energy and electron density. this leads to the relation stated below:

$$\theta_c \propto \sqrt{Z}/E \tag{4.11}$$

where Z is the atomic number and E is the photon energy. Eq.4.11 implies that critical angle decreases with increasing X-ray energy. Higher atomic number materials provide larger critical angles and better reflectivity at higher energies. The field of view (FOV) of X-ray telescopes operating in the range of 0.1 -10 keV is defined by their grazing angles ($\approx 0.5° - 1°$). Hence, the mirrors are usually coated with high-Z materials like gold, platinum and iridium (**?**).

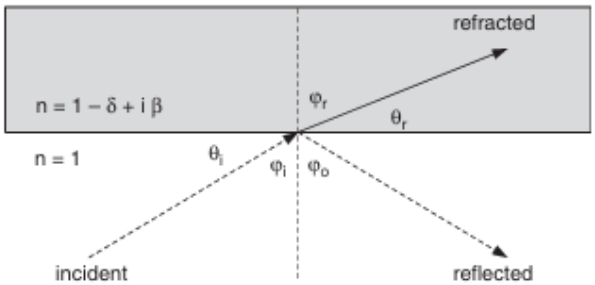

Figure 4.4: Image shows incoming X-ray in a vacuum region (unshaded) coming in contact with a material (shaded) surface of refractive index n at a grazing angle θ_i. θ_r is the angle of refraction.

4.2.1.1 Mirrors

X-ray imaging of cosmic objects usually use paraboloid and hyperboloid shaped mirrors for focusing the radiation incoming from a source (SNRs for example) which has a few arcmin of angular resolution. For a parabolic surface, light rays traveling parallel to the axis of the parabola reflect and converge at a single focal point. The focal length can be set according to the radius of the mirror (R) and grazing angle (α) as $F = R/(2\alpha)$. A single parabolic mirror is not best choice for telescopes as it causes image size to increase linearly with off-axis angles, hence, photons coming from off-axis sources can reach the on-axis image and degrade its quality. A *Kirkpatrick-Baez* configuration is put to use where two parabolic plates are placed orthogonally such that each plate produces one-dimensional focusing but when combined gives a point focus. This type of design is commonly used in synchrotron beam lines but isn't very useful in X-ray astronomy due to a small collecting area and longer focal lengths. Hence, a different type of configuration is used called the *Wolter's* configurations (Wolter (1952a);Wolter (1952b)). It suggests 3 types of configurations: Type I (concave paraboloid - concave hyperboloid), Type II (concave paraboloid - convex hyperboloid) and Type III (convex paraboloid - concave ellipsoid). Of these, the Wolter Type I mirrors are widely used in X-ray astronomy. These mirrors are grazing incidence, coaxial and confocal systems where a paraboloid (P) of revolution around the optical axis is combined with a hyperboloid (H) to form the design (fig.4.5). This arrangement gives it an effective aperture area (A_{eff}) of

$$A_{eff} = 2\pi R\alpha l \tag{4.12}$$

where R is the mirror radius, l is the length of the mirror segment and α (in radians) is the grazing angle. Since α is very small, multiple concentric mirrors (shells) are added giving a larger total area for the interception of the incoming X-ray beams. The intersecting placement of the P and H surfaces allows efficient mounting, nesting of the multiple mirror shells and reduced vignetting. It provides the largest aperture-to-focal-length ratio, ideal for space telescopes, like Chandra or XMM-Newton. A short focal length also helps concentrate photons onto a smaller detector area, improving signal-to-noise ratio for resolved sources.

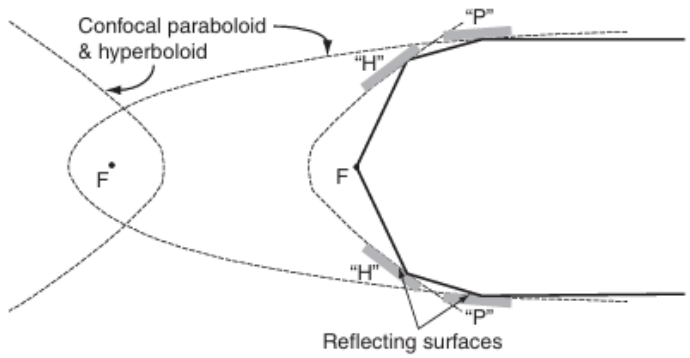

Figure 4.5: Schematic diagram of a Wolter type I mirrors showing an X-ray beam incident on the paraboloid which then reflects off it and hits the hyperboloid proceeding to form an image at one of its focal points (**?**)

4.2.2 X-ray Detectors

After collecting the X-ray photons into our telescope, the nest step is to register them. We need a detector to turn the photon counts into electronic signals and then to data that can be stored and utilized for further analyses. There are various kinds of X-ray detectors in use. This includes proportional counters used in Uhuru, HEAO-1, RXTE and EXOSAT missions. The gas proportional counters detect X-rays photons by ionization in gas. This results in the production of a huge amounts of electrons, hence, providing a measurable pulse which is proportional to the photon energy. There are also gas scintillation proportional counters which use the scintillation light from a noble gas produced during ionization to measure photon energy with improved resolution. Next is the scintillators used in INTEGRAL and Suzaku which produce visible light when struck by X-rays/ gamma-rays which can then be detected by photomultiplier tubes. Fourth, X-ray missions also use micro-channel plates which consist of millions of microscopic channels such that when struck by photons, multiply the electrons producing a detectable signal with a very high spatial resolution. They are used by the Einstein observatory, ROSAT and XMM-Newton. Another type of detectors include micro-calorimeters which measure time temperature increases for every absorbed X-ray photon providing extremely high spectral resolution. We also have CZT (CdZnTe) detectors which belong to the class of semi-conductor detectors used for hard X-ray spectroscopy and imaging. They are in use onboard the Swift, NuSTAR and AstroSat satellites. Lastly we focus on another semi-conductor based detector called the Charge-Coupled Devices (CCDs).

4.2.2.1 CCD Detectors

Charge-Coupled Devices (CCDs) are used in many X-ray missions like ASCA, Chandra, XMM-Newton, Swift and Suzaku. A CCD consists of a grid of interconnected pixels that behave as capacitors. They are arranged on a semiconductor substrate typically made from high-purity silicon. Metal (Gate) electrodes are place above the semiconductor that create a potential well when voltage is applied (fig.4.6). When a photon enters the silicon material, it interacts with the semiconductor lattice and generates an electron-hole pair if the photon energy exceeds

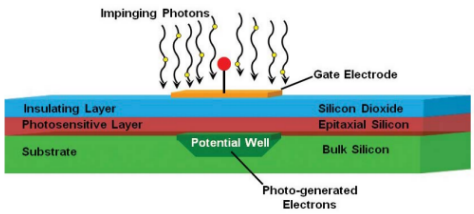

Figure 4.6: General structure of a CCD (Heintz (2019))

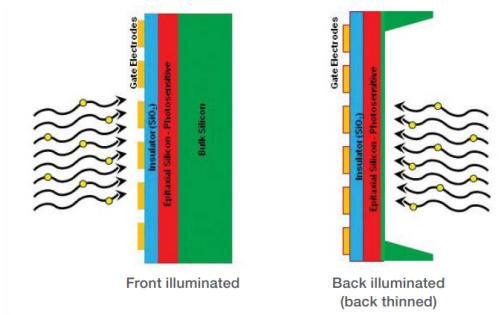

Figure 4.7: Image showing the difference in the structures of front (left) and back (right)-illuminated CCDs (Heintz (2019))

the silicon bandgap ($\sim$ 1.1 eV). This generated electric field separates the charge carriers such i.e. the electrons are collected in the potential wells while the holes migrate towards the substrate and recombine. The number of collected electrons in each pixel is proportional to the number of photons detected. Charges get accumulated in the potential wells of each pixel. Each pixel is electrically linked to the next one, hence, enabling the accumulated charge to be passed sequentially from one pixel to another. The charge moves step by step from the point of photon interaction to a readout amplifier. The amplifier measures the charge and converts it into a digital signal. The ability of the detector to convert photons into electrons gives the measure of its *Quantum Efficiency* (QE). It is defined as the ratio of number of electrons collected to the number of incident photons. While standard CCDs give a QE of 50-60%, CCDs used in the scientific instruments (like telescopes) have a QE $>$ 90%. This is because they are back-illuminated meaning that some of the bulk of the silicon substrate is removed to provide the photons arriving through the back of the sensor access to the photo-sensitive region (fig.4.7) (Heintz (2019)). CCDs make for an important component for high-precision science instruments. They also provide low readout noise, uniform pixel response and high sensitivity to low strength light.

Chapter 5

X-ray Data Analysis

5.1 XMM-Newton

5.1.1 The Satellite

The X-ray Multi-Mirror Mission 'Newton' (XMM-Newton) is an X-ray space observatory designed to study the hot and extreme universe. It is an European Space Agency (ESA) mission funded by the ESA member states and the USA (NASA). It was launched on December 10, 1999 and was then placed into a 48-hour elliptical orbit around the earth inclined at -40 degrees. The perigee is 7000 km and apogee is 114000 km. The lowermost part of the orbit lies within the radiation belts, hence, its operation altitudes are limited to $\geq$ 60000 km. The satellite weighs 4 tonnes and spans a length of 10 m (16 m including the solar arrays), which makes it the biggest satellite ever built in Europe. The spacecraft is designed with a three-axis stabilization and a high pointing accuracy of 0.25 arcsec over a 10 sec interval. The satellite consists of a service module carrying the X-ray mirror modules, propulsion and electrical systems, a long carbon fibre telescope tube ($\sim$ 7 m) and the focal plane assembly carrying the science instruments (Jansen et al. (2001)). There are six science instruments onboard the XMM-Newton namely (fig.5.1a):
(i) three European Photon Imaging Cameras (EPICs) i.e.two EPIC-MOS and a EPIC-PN, equipped inside three telescopes,
(ii) two Reflecting Grating Spectrometer (RGS) on the two EPIC-MOS telescopes, for high-resolution X-ray spectroscopy and spectro-photometry and
(iii) one Optical Monitor (OM) which is an optical/UV sensitive telescope used for optical/UV imaging and grism spectroscopy (see XMM-Newton SOC (2025)).

5.1.2 The Telescope

The three XMM-Newton X-ray telescopes consist of: the mirror assembly door, the entrance baffle, the X-ray baffle, the mirror module, an electron deflector, the Reflection Grating Array (in two out of the three telescopes) and an exit baffle (see fig.5.1b). Some of the important parts are discussed below.

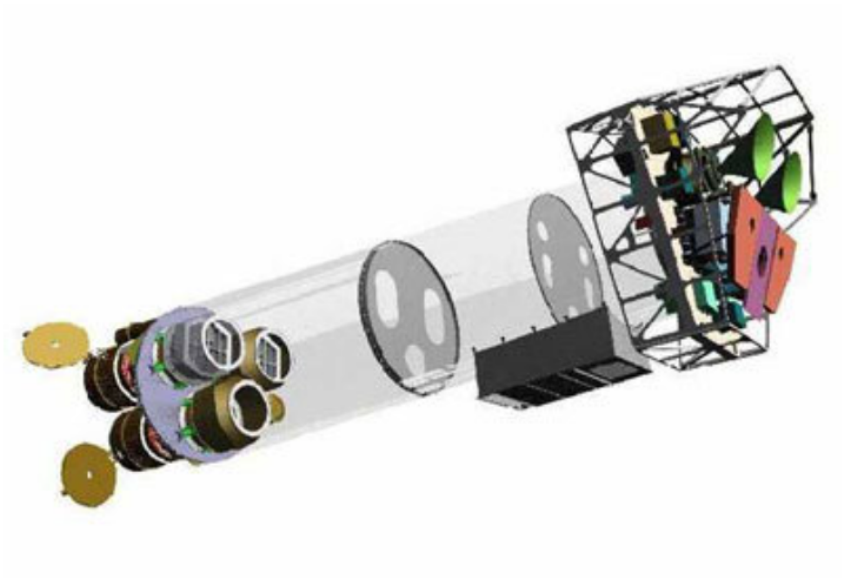

(a)

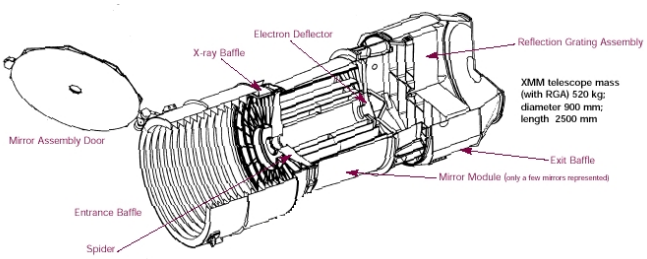

(b)

Figure 5.1: (a)Schematic of the XMM-Newton spacecraft with the mirror modules in the lower-left and X-ray instruments in the right. It shows the EPIC-MOS cameras and radiators (green/black 'horns'), EPIC-PN camera radiator (violet), RGS detectors (pink) and radiators (light blue) and the OM telescope (orange) [Image credit:Dornier Satellitensysteme GmbH (DSS)]. (b) schematic of the X-ray telescope (de Chambure et al. (1999))

5.1.2.1 Mirror Modules

The three X-ray telescopes on the satellite consist of 58 Wolter I (grazing-incidence telescope) mirrors (subsect.4.2.1.1) nested coaxial and confocally. This arrangement provides a large effective collecting area over a wide energy band. The grazing incidence angles of the mirrors ranges from 17 to 42 arcmin. The focal length of the mirror is 7.5 m and provides a resolution of 16 arcsec. They were constructed from superpolished gold coated mandrels using a nickel electroforming technique (de Chambure et al. (1999)). The grazing angles and material of the mirrors make sure that the X-rays are reflected towards a focal point, and not absorbed. The thickness of the smallest (diameter= 306 mm) and the largest mirror (diameter= 700 mm) is 0.47 mm and 1.07 mm respectively, with a minimum separation of 1 mm between adjacent shells. The thinner the mirror shells and the narrower the shell spacing, the larger is the collecting area. The 58 mirrors in each telescope are bound on their entrance aperture to the 16 spokes of a spider as shown in fig.5.2a. An electron deflector is placed at the exit aperture which produces a circumferential magnetic field that prevents low energy electrons reflected by the mirrors from reaching the detector's focal plane (Jansen et al. (2001)). The mirrors show maximum efficiency in the energy range 0.1 to 10 keV.

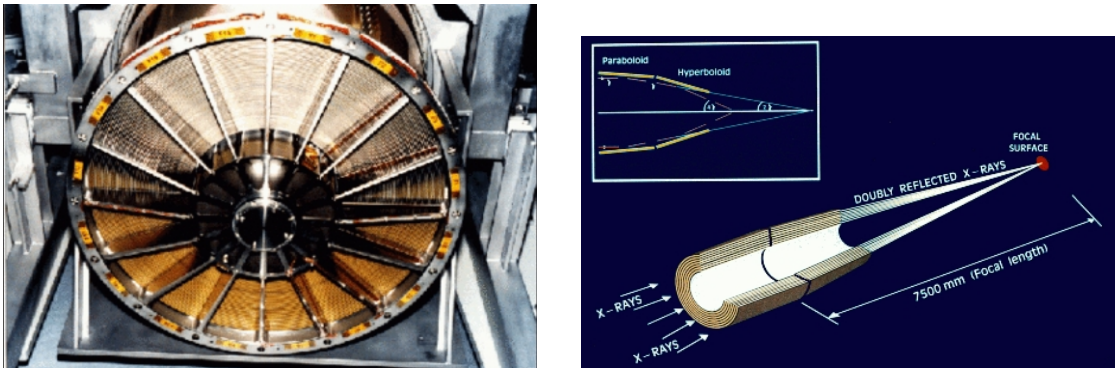

(a) (b)

Figure 5.2: Image (a) shows the structure of the mirror modules in the X-ray telescopes and (b) shows the light path in a telescope with the EPIC-PN camera in its primary focus. [XMM-Newton SOC (2025)]

5.1.2.2 X-ray baffle

The X-ray baffles consist of two sieve-plates made out of circular strips and placed in front of the mirrors coaxially. Each sieve-plate consists of 59 circular strips and 16 radial spokes and is 1 mm thick. The two sieve-plates are placed 84 mm and 145 mm from the mirrors. All its mirror facing surfaces are blackened. They essentially solve the problem of "straylight" that is caused by the single reflections of light, caused by the X-rays coming from objects located close to but off the edge of the Field of View (FOV i.e. cone angle of 15 arcmin), off the hyperboloid section of the mirror shells. They act as collimators and reduce the straylights.(de Chambure et al. (1999))

5.1.3 EPIC

The main instrument of interest on XMM-Newton is the European Photon Imaging Camera (EPIC). The three X-ray telescopes have three EPIC instruments: two MOS (Metal Oxide Semi-conductor) CCD arrays and a PN CCD camera. The EPIC cameras allow us to perform sensitive imaging observations over the 30 arcmin FOV of the telescope in the energy range of 0.15 to 15 keV with moderate spectral ($E/\Delta E \sim 20 - 50$) and angular ($\sim 6''$ FWHM) resolution. The CCDs work in a photon counting mode. The camera working modes can be selected from the Full Frame, Extended Full Frame, Large/Small Window, Partial Window, Timing and the Burst modes. The EPIC cameras are also provided with aluminized light/UV blocking filters on a 6-position filter wheel. There are four filters (two thin, one medium and one thick) per camera (Villa et al. (1998)). The other two filter wheel positions are occupied by the closed and open positions.

5.1.3.1 EPIC-MOS

The EPIC- Metal Oxide Semi-conductors (MOS) is made up of seven EEV type 22 front-illuminated CCDs placed in the focal plane of each MOS camera in an arrangement shown in fig.5.7. The central CCD is positioned at the focal point of the optical axis and the outer six CCDs are placed 4.5 mm towards the mirror to be approximately along the focal place curvature and improve off-axis source focusing. This creates a dead space (<300 µm) between them. This space is minimized by stepping the adjacent CCDs by around 1 mm to overlap by 300 µm. The EEV type 22 CCD is a three-phase frame transfer device made of high resistivity epitaxial silicon with an open-electrode structure with a useful quantum efficiency in 0.2 to 10 keV range. It gives an imaging area of $\sim$ 2.5 x 2.5 cm such that the arrangement of the seven CCDs cover the focal plane (diameter = 62 mm). The imaging section has 600 x 600, $40\mu m^2$ pixels and each pixels span 1.1 x 1.1 arcsec of the FOV. The EPIC-MOS CCD arrays are located behind the X-ray telescopes equipped with the RGS. Almost only 44% of the incident flux reach the MOS cameras as the RGS gratings divert the rest towards them. Note that MOS1-CCD3 and CCD6 were not usable due to a micrometeorite impact event, scattering debris into the focal plane, in December 2012 and March 2005 respectively. This can be seen in the case of one of our SNRs i.e. SNR G306.3 -0.9 (Table 5.3) under analysis. The cameras are also provided with with a cryogenic cooling system and a MOS radiator to prevent any radiation damage (Turner et al. (2001)).

5.1.3.2 EPIC-PN

The PN camera contain a single Silicon wafer with 12 integrated CCD chips (fig.5.3b). The wafer is manufactured with extreme precision to maintain the very high resistivity of the 300µm -thick double-sided processed silicon detectors. This makes it possible for it to efficiently ($\sim$ 90% from 0.5 to 10 keV) detect the high energy X-rays, unlike the MOS cameras. The imaging section of the PN CCDs has 400 x 384 pixels and imaging area of 36 cm^2 (Strüder et al. (2001)).

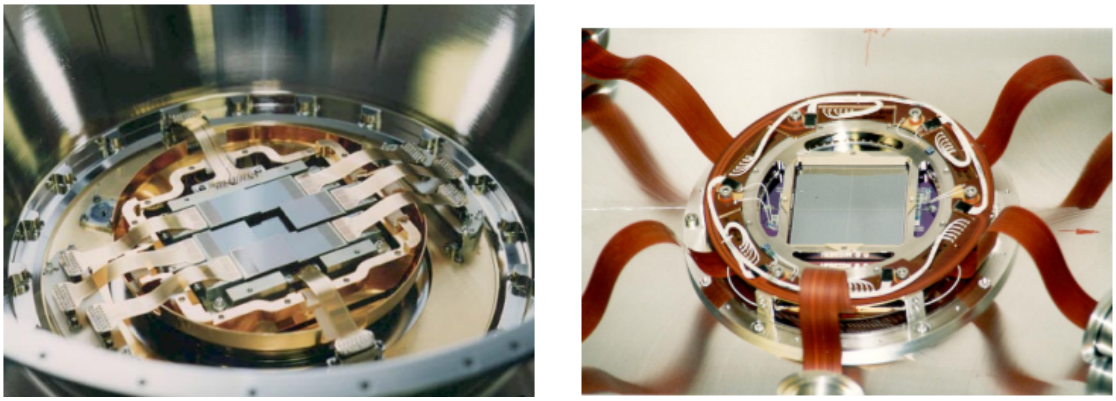

(a) (b)

Figure 5.3: CCDs of the EPIC-(a)MOS and (b)PN cameras [XMM-Newton SOC (2025)]

5.1.4 Data Observation

This section provides details about the XMM-Newton EPIC observations of the three SNRs which would be studied in this thesis. The data is extracted from the EPIC- MOS1, MOS2 and PN instruments (Table 5.1) for the sources: SNR G272.2 -3.2 and SNR G306.3 -0.9. The analysis of SNR G299.2 -2.9 contains data only from the EPIC- MOS1 and MOS2 instruments as the PN data was bad. Note that since the source is very bright, absence of the PN data does not affect our analysis. The other details are mentioned in the table (Table 5.2) below.

Source	MOS1	MOS2	PN	Filter
G272.2 -3.2	S001	S002	S003	Thin1
G306.3 -0.9	U002	U002	U002	Medium
G299.2 -2.9	S001	S002	U002 (n/a)	Medium

Table 5.1: List of EPIC instruments exposure IDs (exp-ID) and filter IDs

Source	ObsID	Obs.Date	RA(°)	Dec.(°)	Exp.(ks)	PI
G272.2 -3.2	0112930101	10.12.2001	136.69	-52.12	36.377	B. Aschenbach
G306.3 -0.9	0691550101	02.03.2013	200.44	-63.58	56.191	J. Miller
G299.2 -2.9	0112890101	24.02.2002	183.83	-65.51	12.727	B. Aschenbach

Table 5.2: List of XMM-Newton observations used for imaging and spectral analysis.The exposure times are calculated as the average exposure times of the three EPIC instruments.

5.1.5 Background

The CCDs in the EPIC instruments on the satellite capture all the photons hitting them.This includes those from the astrophysical objects and the background.The background components originate from certain instrumental, particle and cosmic processes. The various background components are described below:

Cosmic X-ray Background (CXB): The cosmic X-ray background represents emissions from astrophysical objects which are not related to the object of interest. These emissions include Local Hot Bubble (LHB) emissions in the soft band, thermal emissions from the Galactic halo, emissions from unresolved active galactic nuclei (AGN) and solar wind charge exchange (SWCX). This type of diffuse background has to be modeled using absorption powerlaws and thermal plasma models (see subsect.5.4.1).

Solar Wind Charge Exchange (SWCX): This type of background occurs when ions from solar winds interact with exospheric hydrogen near the earth(geocorona) or the neutral interstellar medium (Manconi et al., 2024).This interaction results in the emission of low energy X-ray photons which are recorded as faint, diffuse emission in the detector at energies below 2 keV. The SWCX is then modeled by analyzing the spectral shape of this soft emission.

Instrumental Background: This type of background is comprised of the quiescent particle background (QPB), soft proton flares (SPF), instrumental fluorescence lines, straylight (5.1.2.2) and other electronic noise and detector artifacts.

The Quiescent Particle Background (QPB): It is an instrumental background caused by high energy particles (predominantly protons) passing through the telescope and interacting with the detectors, making an inherent and stable background. It appears as a flat,continuous emission and fluorescent instrumental lines. The QPB is modeled using the Filter Wheel Closed (FWC) data taken during closed filter observations, such that any X-rays from outside the instrument and the soft protons are blocked, and the corner data collected by the CCD pixels outside the FOV as explained in Kuntz and Snowden (2008).

Soft Proton Flares (SPF): This background is caused by low energy(soft) protons falling onto the detectors characterized by sudden bursts of high background count rates.The SPF is modeled using the task `espfilt` in the XMM-ESAS that works by removing the time intervals that show high proton activities.

Instrumental Fluorescence Lines: Particles hitting the detectors sometimes interact and excite the detector materials producing characteristic emission lines. Some notable lines include Al-Kα ($\sim$ 1.49 keV) and Si-Kα ($\sim$ 1.74 keV). These lines are modeled explicitly during spectral fitting.

5.2 Data reduction and processing

The use of XMM-ESAS (XMM-Newton Extended Source Analysis Software) package has been incorporated for the processing of the data. It provides us with the tools required for imaging and spectral analysis of extended sources and diffuse emissions. It lets us model the Quiescent Particle Background(QPB) for spectral

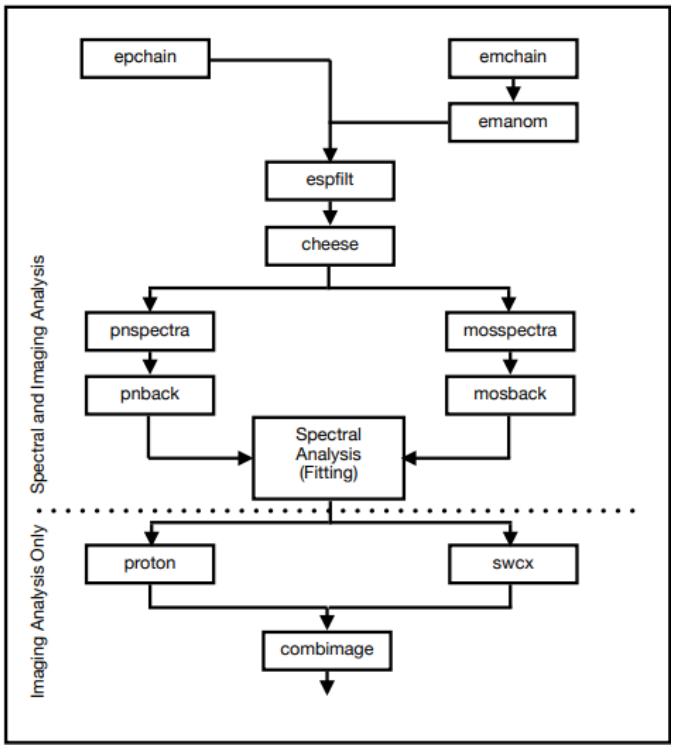

Figure 5.4: Flow chart for the general ESAS processing of XMM-Newton EPIC data (Snowden and Kuntz, 2023)

analysis and allows the creation of background subtracted, exposure corrected images of objects of interest. The following Science Analysis System(SAS) tasks, as described in the XMM-ESAS Cookbook (Snowden and Kuntz, 2023), were used to obtain the final spectra and images of the three Supernova Remnants(SNRs). The processing begins with loading SAS `version 21` as a module. It should be noted that, though most of the tasks were performed with SAS v21, few tasks required SAS v20. Once SAS is loaded onto the working terminal, we start by recreating the event files. The further tasks can be visualized as shown in fig.5.4.

`emchain` and `epchain`: The task `emchain` produces event files for all the CCDs of MOS1 and MOS2 and `epchain` for PN. The task creates multiple (`.FIT`)files of which `*EVLI*.FIT` is of importance to us. The `.FIT` here refers to Flexible Image Transport System(FITS), which is the standard format of files used by ESAS.

`emanom`: This task reads a MOS event file and calculates the (2.5-5.0 keV)/(0.4-0.8 keV) hardness ratio from the corner data for each CCD to determine whether a chip is in an anomalous state i.e. if it has anomalously high Quiescent Particle Background(QPB) at energies below 1.0 keV. It creates an output log file (e.g.mos2S002-anom.log) where the anomalous states are flagged as Good(G), Intermediate(I), Bad(B), Off(O) or Undetermined(U). Only the CCDs flagged Good(G) are further used for the analysis. The table 5.3 below shows the status of the CCDs (2 to 7) used in our observations.

`espfilt`: This next task is used for filtering the Soft Proton Flare (SPF) (defined in sect.5.1.5). It creates light curves for both the Field Of View (FOV) and the corner data in the energy range $2.5 - 8.5$ keV and creates an X-ray count rate histogram from the FOV data. This histogram typically has a roughly Gaussian

Source	MOS1	MOS2
G272.2 -3.2	GGBIGG	BGGGGG
G306.3 -0.9	GOIGOG	GGGGGG
G299.2 -2.9	GGBGGG	GGGGGG

Table 5.3: list of the anomalous states of CCDs (2 to 7) of the EPIC-MOS1 and MOS2 instruments flagged as Good(G), Intermediate(I), Bad(B) or Off(O).

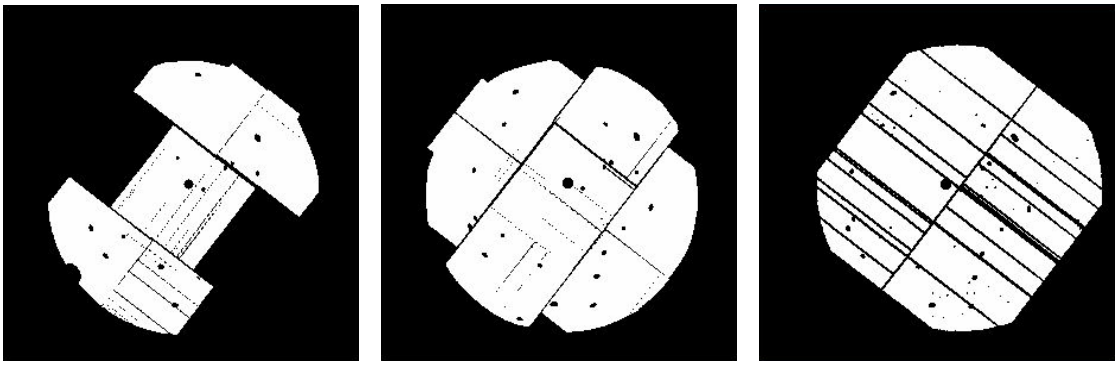

Figure 5.5: cheese mask images of MOS1(*left*), MOS2(*middle*) and PN(*right*) of SNR G306.3-0.9

peak. The task fits a gaussian to this peak and determines the thresholds at $\pm 1.5\sigma$. It then creates a Good Time Interval (GTI) file for the time intervals with count rates within this threshold.

`cheese`: This task is used to detect and excise point sources from our X-ray images and spectra. It does this by running the `edetect_chain` task which detects point sources in the FOV of both the PN and MOS detectors. Next, it generates a mask file that removes these point sources while keeping the surrounding diffuse emission, hence looking like a "Swiss-cheese" mask. The mask images of the MOS and PN detectors of the source SNR G306.3 -0.9 are shown in fig.5.5 as an example.

`mosspectra/pnspectra and mosback/pnback`: These tasks are used for the creation of the quiescent particle background (QPB) spectra. The spectral information is extracted from: the corner spectra from each (non-anomalous) chip of the observation being analyzed, the corner spectra from each chip of the FWC data and the FOV spectra from each chip of the FWC data. The FWC provides the spatial distribution of the QPB events, while the corner data provide a measure of the normalization of the QPB rate and shape of the QPB spectrum. The tasks `mosspectra` and `pnspectra` extract these data of the MOS and PN instruments respectively. The first images and spectra are extracted for the full FOV in three energy bands(RGB): 0.3-0.7 keV (soft, in Red), 0.7-1.1 keV (medium, in Green), 1.1-4.2 keV (hard, in Blue). To maintain consistency and comparability between the three SNRs, the energy bands are kept the same. The tasks `mosback` and `pnback` are used next which combine all the extracted data into the QPB spectrum and images in the given bands.

The image files (`*fovimsky*.fits`) for the three energy bands created in this step are then viewed using the `DS9` image viewing application. The next step

involves selecting a region to extract the source and the background data for further analysis. The selected source and background regions, for the three SNRs, from which the final images and spectra would be created are shown in fig.5.6. The centers of the source regions are given in table.5.4. These regions are saved as `.reg` files and later need to be converted to `.txt` files. The `mosspectra/pnspectra and mosback/pnback` tasks are run again, for the source and background regions separately for each energy band. It should be noted that the selected regions need to be converted from sky coordinates to detector coordinates before this task. Also, the output files created after running these tasks need to be renamed or moved to a different folder to avoid overwriting each time.

Source	center	
	R.A. (2000)	Dec. (2000)
G272.2 -3.2	$09^h06^m47^s$	$-52°05'53''$
G306.3 -0.9	$13^h21^m49^s$	$-63°33'40''$
G299.2 -2.9	$12^h14^m51^s$	$-65°28'53''$

Table 5.4: center coordinates (RA and Dec. in J2000) of the source regions selected for imaging and spectral analysis of the three SNRs.

`grppha`: Many times for chi-squared statistics the data is very sparse to be useful for spectral fitting, especially at higher energies. Hence, the data is binned. This task groups different spectral channels to ensure a minimum number of counts per bin and improves the signal-to-noise ratio. In our case, the data will be grouped with a minimum of 50 counts per channel.

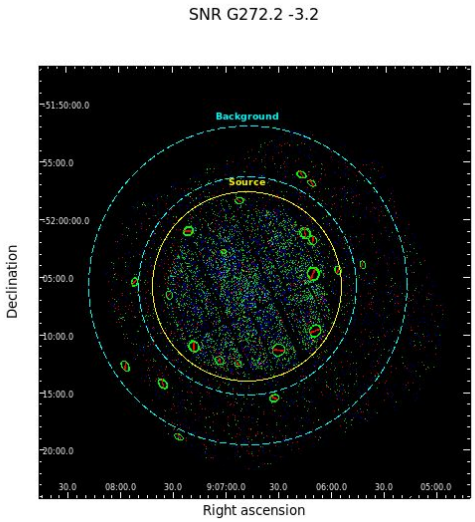

(a)

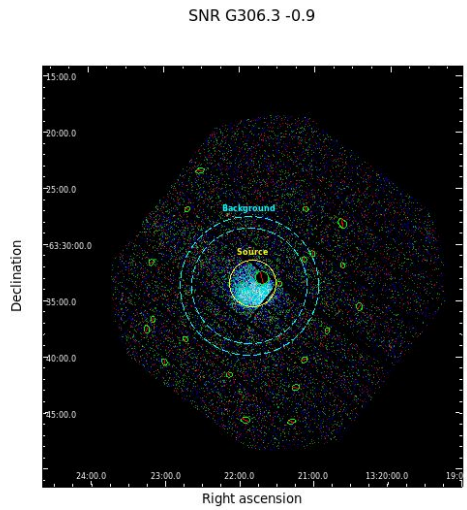

(b)

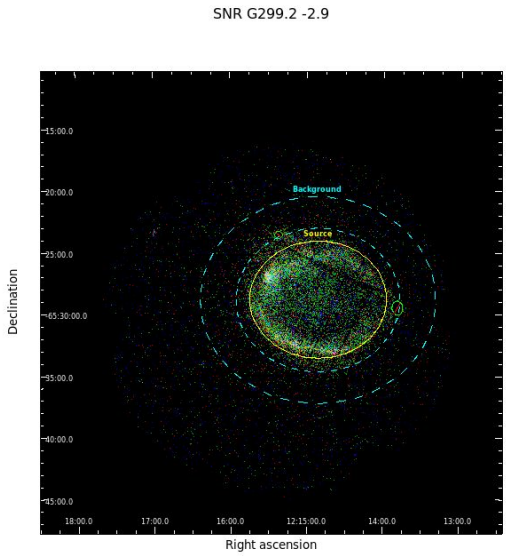

(c)

Figure 5.6: Output RGB images from mosspectra/pnspectra task (a),(b)and (c) of SNR G272.2 -3.2, SNR G306.3 -0.9 and SNR G299.2 -2.9 respectively showing region selection. The source (yellow) region is depicted as a circle (or ellipse (c)) while the background (cyan) region is selected in the vicinity of the source shown as a dashed annulus (or elliptical annulus (c)). The regions marked in green, with a red line, are the point sources excised using the `cheese` task. The X-ray colors correspond to 0.3-0.7 keV (red), 0.7-1.1 keV (green) and 1.1-4.2 keV (blue). The image is set in a logarithmic scale.

5.3 Image Analysis

The aim here is to obtain a clear image of the object of interest, which implies removing the background contaminations from our data. Modeling of the backgrounds mentioned in sect.5.1.5 essentially requires spectral fitting of the entire FOV. Hence, the imaging depends mainly on spectral fitting to obtain a good background subtracted image.
At this point in the analysis, some low-energy proton background can still exist. The next step here is to remove residual SPF contamination, if any, from the observational data. This is done by spectral fitting the entire FOV by including a (broken)powerlaw component in the model. Since soft protons are not vignetted like X-ray photons, their background must be scaled separately. This scaling factor can be obtained using the task `protonscale`. The fit gives us the normalization(`pnorm`) in counts $keV^{-1}s^{-1}$and the powerlaw index(`pindex`) expressed as negative photon index in `XSPEC`. These values are then used in the next task.

`proton`: This task generates maps of the soft proton contamination in our observation. Its input parameters include an image file in detector coordinates and a spectrum file which must be the one used in the spectral fit where the magnitude of the residual SPF contamination was determined. It also requires the pnorm and pindex values from the FOV spectral fit. The task is run separately for the MOS and PN instruments in each of the selected energy bands. The task produces output in detector coordinates.

`rotdet2sky`: The output images from the previous task need to be converted to sky coordinates to be useful to us. The task performs a reflection, an offset and a rotation for this conversion. The same task has to be repeated for the QPB images.

By now, all the main backgrounds (QPB and SPF) have been subtracted and the exposures corrected. The next step is to combine all the data from the different instruments. This is done by the following task.
`combimage`: This task adds the individual components from the three instruments (MOS1, MOS2 and PN) with proper scalings for different filters and different instruments and also from multiple exposures from the same ObsID.

`binadapt`: This next step combines all the components and provides adaptive smoothing and binning to produce a final good-looking image of the SNRs. In this analysis the `binning` is set to 2 pixels and the `smoothingcounts` to 50 i.e. a gaussian kernel of 50 counts is applied for the adaptive smoothing of the image. Smoothing helps to reduce certain noise fluctuations.

At the end of this step, the background-subtracted and exposure-corrected image is ready and can be viewed using DS9 (figs.5.7, 5.8 and 5.9). The images are generated using linear scale instead of the generally used logarithmic scale due to high brightness of the sources.

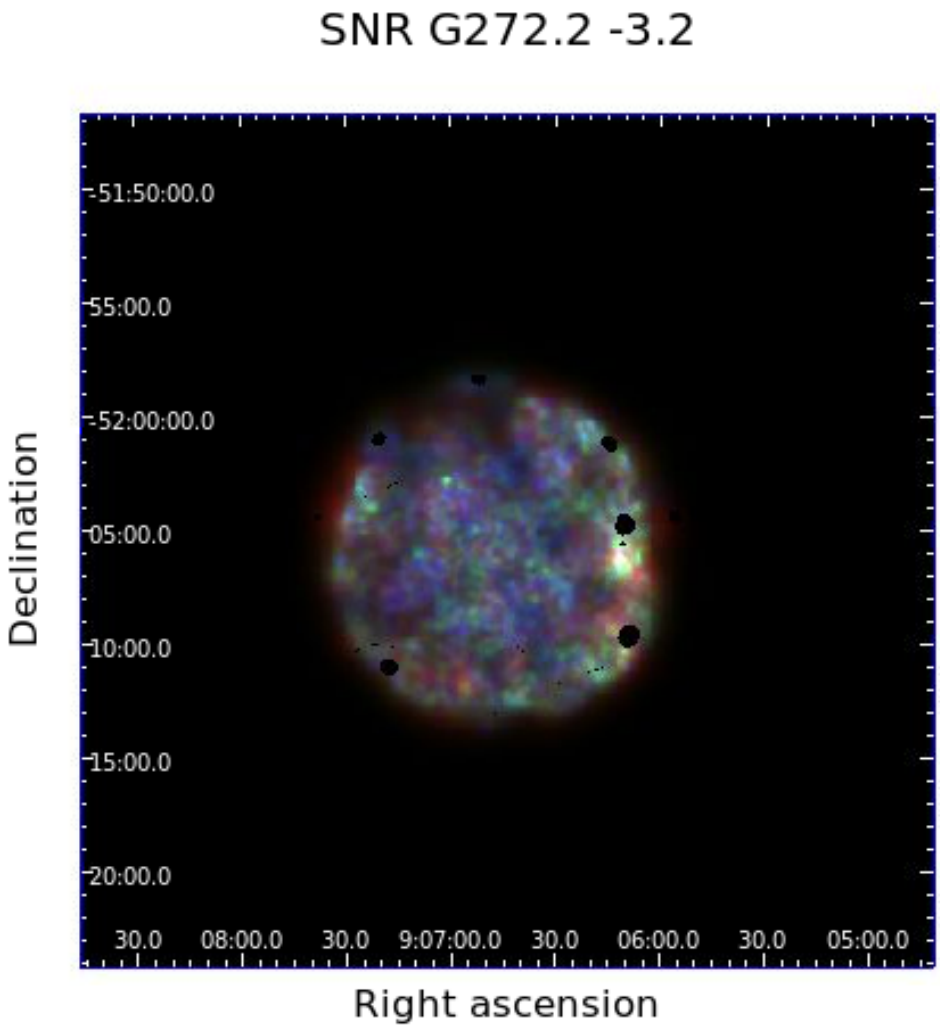

Figure 5.7: XMM-Newton background-subtracted and exposure corrected RGB image of SNR G272.2 -3.2. The X-ray colors correspond to 0.3-0.7 keV (red), 0.7-1.1 keV (green) and 1.1-4.2 keV (blue). The coordinates (RA. and Dec.) refer to epoch J2000

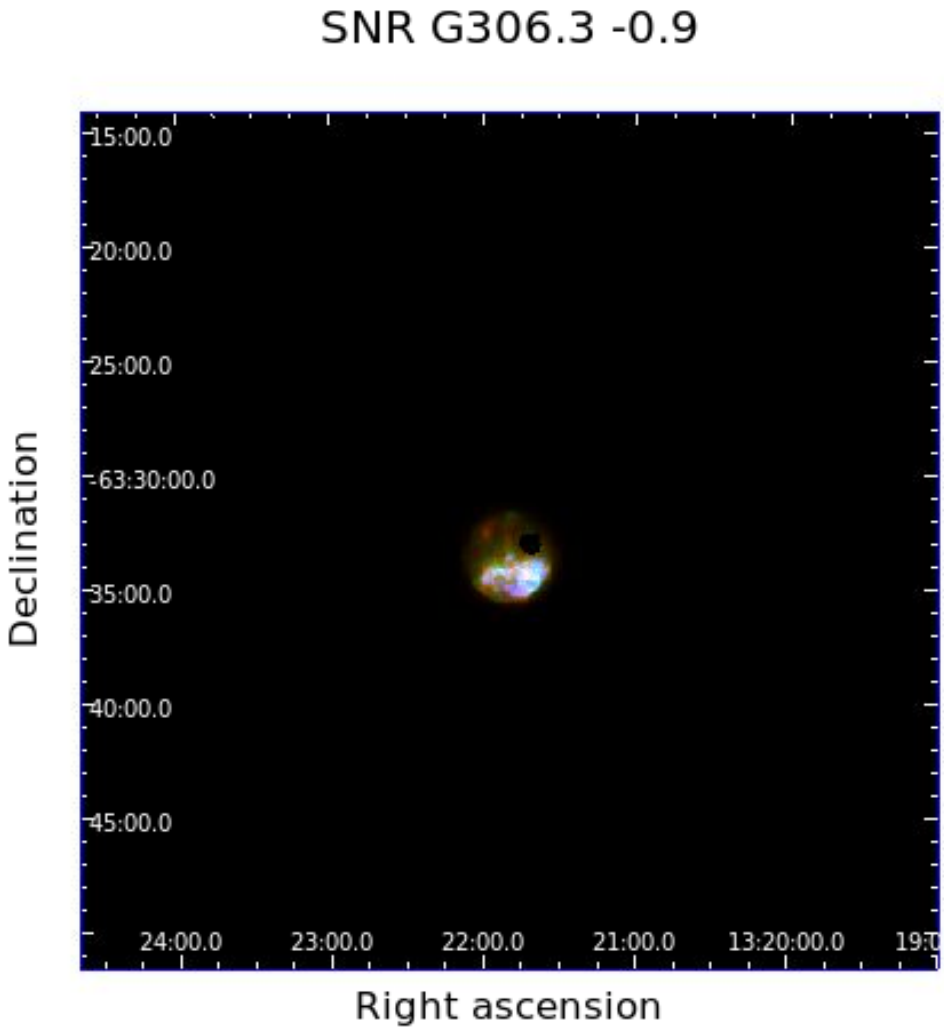

Figure 5.8: XMM-Newton background-subtracted and exposure corrected RGB image of SNR G306.3 -0.9. The X-ray colors correspond to 0.3-0.7 keV (red), 0.7-1.1 keV (green) and 1.1-4.2 keV (blue). The coordinates (RA. and Dec.) refer to epoch J2000

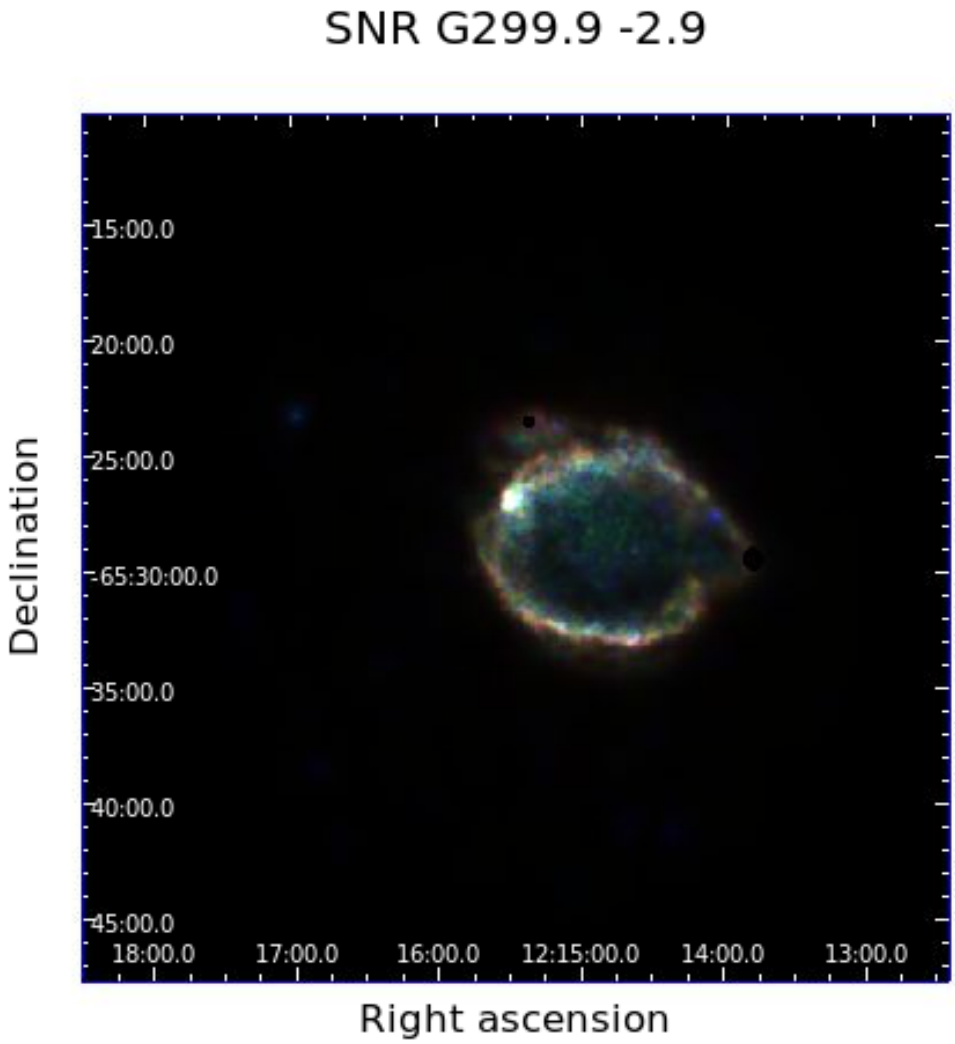

Figure 5.9: XMM-Newton background-subtracted and exposure corrected RGB image of SNR G299.2 -2.9. The X-ray colors correspond to 0.3-0.7 keV (red), 0.7-1.1 keV (green) and 1.1-4.2 keV (blue). The coordinates (RA. and Dec.) refer to epoch J2000

5.4 Spectral Analysis

The next major part of our study is the spectral fitting of the data. First, different background components (both instrumental and cosmic) need to be fitted. These components can vary with time, observation direction on the sky, detector position, location of the satellite in its orbit and the location of earth in its orbit. Once these components are fitted, we can finally proceed to the spectral fitting of the source under study. This is done by spectral fitting the background data taken from an area around the source as shown in fig.5.6. These fit values are then included in the spectral fitting of the source of interest. All the spectral fitting is done using `XSPEC` (Arnaud (1996)) version 12.15.1. The abundances in the fitting models are set to `wilm` (Wilms et al. (2000)). The χ^2-statistics is used to determine the best-fit models in this analysis.

5.4.1 Background Modeling

The modeling is based on the methodologies of Snowden et al. (2008) and Snowden and Kuntz (2023). All the models were multiplied with their corresponding extraction area ($arcmin^2$) for normalization. The backgrounds for all the three SNRs are fitted using the same model as stated below. Both X-ray and non-X-ray backgrounds are included in this model.

Background model:

```
constant<1> (gaussian<2> + gaussian<3> + gaussian<4> + gaussian<5> +
gaussian<6> + gaussian<7> + gaussian<8> + gaussian<9> + apec<10> +
TBabs<11> (apec<12> + apec<13> + TBabs<14>* powerlaw<15>))
```

The X-ray backgrounds include the local bubble, the hot and the cold Galactic halo and an extragalactic background component. To account for the thermal emissions from the Local Hot Bubble (LHB), an unabsorbed thermal component, APEC (10) (Atrophysical Plasma Emission Code given by AtomDB 3.1.3), was used with the temperature fixed at kT = 0.1 keV. Two absorbed thermal components APEC (12 and 13) were used to represent the emission from the cold- and hot-Galactic halo with temperatures in the range kT=0.1-0.2 keV and kT= 0.7-0.8 keV respectively, for the three SNRs. The Galactic absorption component, TBABS (11), was also added with the absorbing column density $(N_H)_{gal.}$ fixed to the value obtained from the H_I map (HI4PI Collaboration et al. (2016)) using the N_H tool by HEASoft. The extragalactic component (TBABS (14)) is not contributing in the scenario of our study as our sources are in the same galaxy (Galactic SNRs), hence, the absorption $(N_H)_{extragal.}$ was set to 0. The POWERLAW (15) component was added to account for the non-thermal emissions from extragalactic or unresolved X-ray sources (CXB). The photon index is fixed at $\Gamma = 1.46$ (Chen et al. (1997); Kuntz and Snowden (2000)). The norms for these components were kept free for spectral fitting.
The model also consists of GAUSSIANs (2-9) to account for the possible SWCX contamination by fitting the lines: C VI (0.37 keV), C VI (0.46 keV), O VII(0.57 keV), O VIII (0.65 keV), O VIII (0.81 keV), Ne IX (0.92 keV), Ne IX (1.02 keV)

and Mg XI (1.35 keV). They were fitted at zero width with free normalizations. The instrumental EPIC background for each instrument (MOS1, MOS2 and PN) were fitted separately using gaussians at 1.49 keV and 1.75 keV for Al-K and Si-K fluorescence lines respectively. For PN, the Si-K line was not required. Other instrumental lines at higher energies were also fitted to get a good fit. The instrumental gaussians are modeled along with a powerlaw component that accounts for the SP contamination for which the data is taken from the 'diagonal response files'.The fitted background spectra for the three SNRs are shown in figs.5.10, 5.11 and 5.12 respectively.

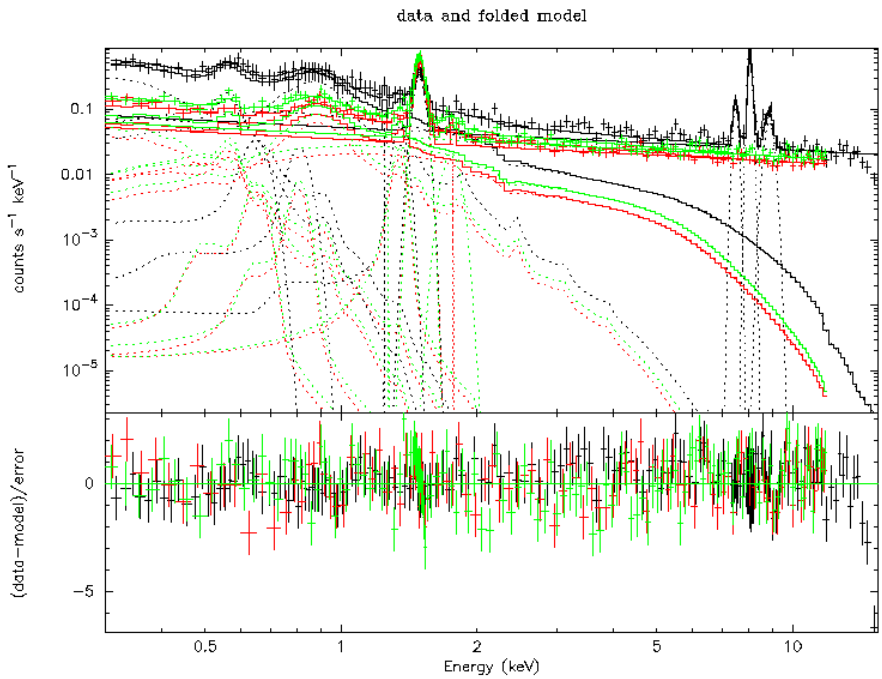

Figure 5.10: Fitted Background spectra of PN, MOS1 and MOS2 data taken from the selected annulus region (5.6a) around SNR G272.2 -3.2

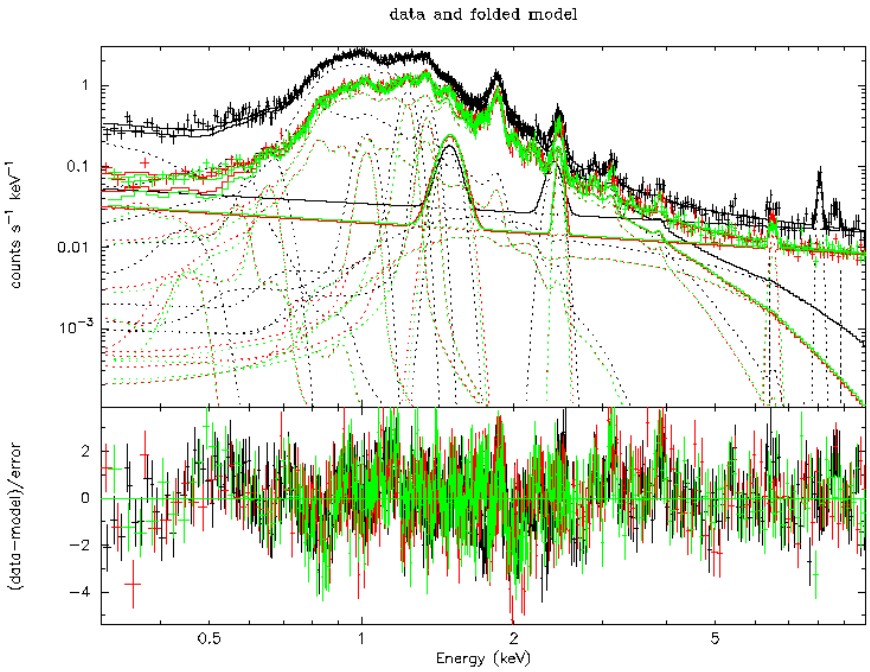

Figure 5.11: Fitted Background spectra of PN, MOS1 and MOS2 data taken from the selected annulus region (5.6b) around SNR G306.3 -0.9

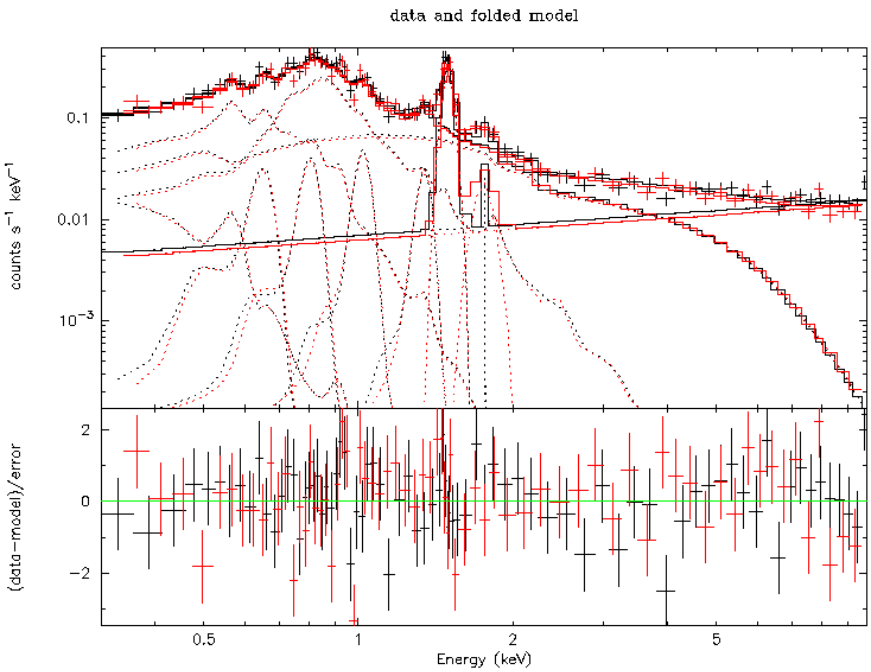

Figure 5.12: Fitted Background spectra of MOS1 and MOS2 data taken from the selected elliptical annulus region (5.6c) around SNR G299.2 -2.9

5.4.2 Source Modeling

The next step now is to model the source spectrum obtained from the selected regions of the three SNRs as shown in fig.5.6. The overall model contains the background components, fitted earlier in subsect.5.4.1, to which the new source components (depicted in brown) are added as shown below.

Background + Source model:

```
constant<1> (constant<2> (gaussian<3> + gaussian<4> + gaussian<5> +
gaussian<6> + gaussian<7> + gaussian<8> + gaussian<9> + gaussian<10>
+ apec<11> + TBabs<12> (apec<13> + apec<14> +
TBabs<15>* powerlaw<16>)) + TBabs<17> (Source))
```

The constant(2) is added to the model to scale or adjust for the differences in the extraction region areas between the source and background. It is taken as the ratio of the areas of source extraction to the background using `BACKSCAL` obtained from the `protonscale` task. The scaling factor is separately determined for each EPIC instrument. Next, TBabs(17) is added as a multiplicative component to the main source components to account for the foreground Galactic absorptions. The component had to be freed later for a better fit. The other source components used in the model for each SNR are described separately.

5.4.2.1 SNR G272.2 -3.2

A thermal emission component was added to model the emission from the SNR. We start with a collisional ionization equilibrium (CIE) plasma model APEC but the best fit for the source spectrum was obtained by using a Variable Non-Equilibrium Ionization (VNEI) model as it allows us to vary the abundances. As stated earlier, solar abundances obtained by Wilms et al. (2000) were used in the model. To get a good fit, the VNEI parameters: *electron temperature* kT (keV), *ionization temperature* τ (s/cm^3) and normalization (norm.) were thawed and fitted. The fit improved but not sufficiently. Another fit was tried with just Fe free among the elements. The fit showed sub-solar abundance of Fe and the statistics were poor. The fit significantly improves when lighter elements (O, Ne, Mg, Si, S) were freed and fit. The model still left an excess at around E$\sim$ 1.2 keV. A gaussian was fitted at E$\sim$ 1.23 keV. This residual is commonly reported in SNR spectral analyses and accounts for the incomplete modeling of the Fe-L line complex (Smith et al. (2001)). Similar fits were obtained in studies of other galactic SNRs like Sato et al. (2016) and Okon et al. (2018). This Gaussian component had to be added in the models of the other two SNRs (G306.3 -0.9 and G299.2 -2.9) as well. The final model components are depicted below. The best fit results with errors calculated using `error` and `steppar` are shown in table.5.5 and the fitted spectrum in fig.5.13

Source model: `gaussian<18> + vnei<19>`

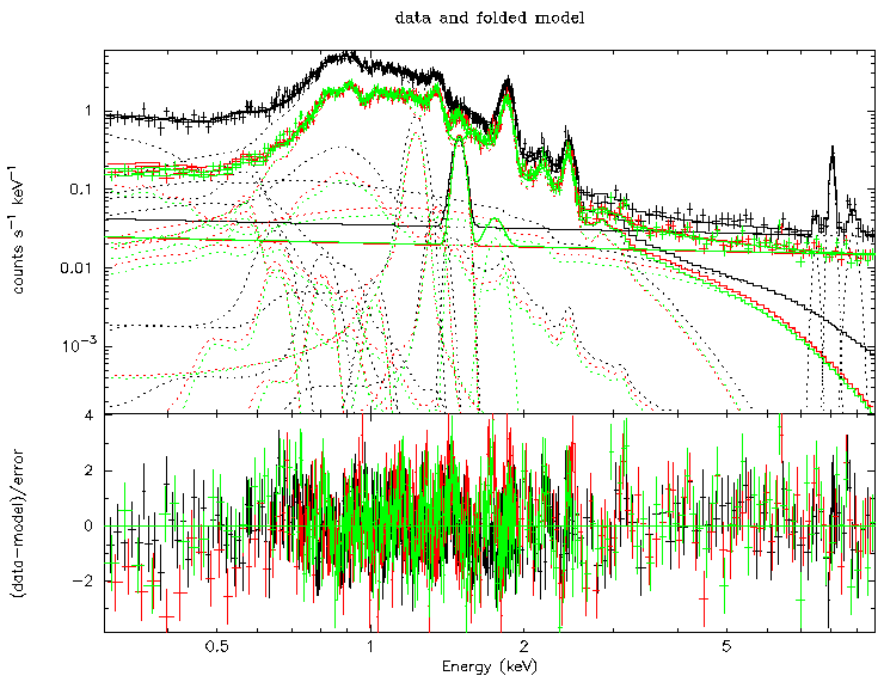

Figure 5.13: Epic spectra of PN, MOS1 and MOS2 data taken from the source region of the SNR G272.2 -3.2 and its best fit model. The solid lines show the main source components (VNEI + GAUS) while the dotted and dashed lines comprise of all the other model components. The lower panel shows delta χ^2-error statistics of the fit.

5.4.2.2 SNR G306.3 -0.9

A similar approach was adopted for the spectral fitting of this source. We start with the CIE APEC model. The electron temperature (kT) and norm. parameters were freed to fit. The result still leaves residuals around prominent emission line complexes. Hence, a second model with component like APEC, NEI, VAPEC and VNEI was tried for the fit. The best fit from the different combinations was obtained by a two component plasma model using APEC and VNEI. The VNEI model had higher elemental abundances in the heavier zone (Si, S, Ar, Ca, Fe, Ni) with a notably high value of Calcium (Ca) abundance (see table.5.5). The Ni abundance is fixed to Fe. The VNEI has a higher electron temperature kT$\sim$1.03 keV depicting its association with the ejecta material. The APEC on the other hand is a cool component with kT$\sim$ 0.21 keV representing emissions from plasma close to ionization equilibrium. A residue around $E \sim 1.22$ keV was found and fit with a gaussian as mentioned in the SNR G272.2 -3.2 spectral fit. The final source model is mentioned below. The best fit spectrum is shown in fig.5.14 and the fit parameters in table.5.5.

Source model: `gaussian<18> + apec<19> + vnei<20>`

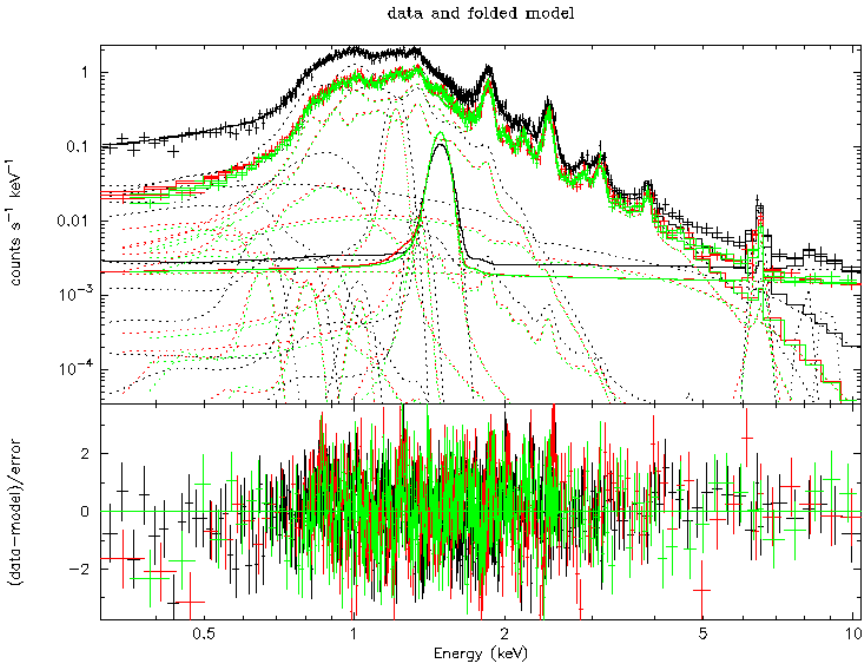

Figure 5.14: Epic spectra of PN, MOS1 and MOS2 data taken from the source region of the SNR G306.3 -0.9 and its best fit model. The solid lines show the main source components (APEC + VNEI + GAUS) and the dotted and dashed lines show the other components in the model respectively. The delta χ^2 fit statistics are shown in the lower panel.

5.4.2.3 SNR G299.2 -2.9

The source spectrum of this SNR was fit using different models as described in the previous two SNRs. The best fit was obtained with a combination of a gaussian accounting for the line at $E \sim 1.23$ keV and a VNEI model. The abundances were predominantly higher for the heavier element group. Ni shows high abundance here and could not be constrained to the Fe values to get better fit statistics. Since the image of the SNR (fig.5.9) clearly shows a shell structure (shells usually contain materials shocked at different times), a VPSHOCK model was also tried for the fitting instead of the VNEI model. Yet the best fit was was obtained with the VNEI model. The final fit model is stated below with the fiited spectrum shown in fig.5.15.

Source model: `gaussian<18> +vnei<19>`

Parameters	G272.2 -3.2	G306.3 -0.9	G299.2 -2.9
Model	GAUS + VNEI	GAUS + APEC + VNEI	GAUS + VNEI
$N_H(10^{22}\,cm^{-2})$	$1.31^{+0.06}_{-0.06}$	$2.10^{+0.04}_{-0.04}$	$0.60^{+0.02}_{-0.03}$
$kT_{apec}(keV)$	-	$0.21^{+0.01}_{-0.01}$	-
$kT_{vnei}(keV)$	$0.61^{+0.04}_{-0.03}$	$1.03^{+0.06}_{-0.05}$	$0.45^{+0.03}_{-0.02}$
O	$0.47^{+0.18}_{-0.15}$	-	-
Ne	$1.08^{+0.15}_{-0.13}$	-	-
Mg	$0.93^{+0.06}_{-0.05}$	-	-
Si	$2.50^{+0.15}_{-0.14}$	$2.43^{+0.22}_{-0.20}$	$3.67^{+0.25}_{-0.26}$
S	$3.13^{+0.42}_{-0.38}$	$2.98^{+0.25}_{-0.22}$	$10.44^{+2.21}_{-0.99}$
Ar	-	$3.48^{+0.48}_{-0.54}$	$8.35^{+4.75}_{-4.63}$
Ca	-	$8.18^{+1.50}_{-1.57}$	-
Fe	-	$3.94^{+0.39}_{-0.34}$	$1.03^{+0.06}_{-0.04}$
Ni	-	$3.94^{+0.39}_{-0.34}$	$7.69^{+0.56}_{-0.55}$
$\tau\,(cm^{-3}s)$	$5.85^{+0.69}_{-0.61} \times 10^{10}$	$1.05^{+0.18}_{-0.15} \times 10^{11}$	$3.24^{+0.37}_{-0.37} \times 10^{10}$
$Norm_{gaus}(10^{-4})$	$4.53^{+0.51}_{-0.47}$	$5.45^{+0.48}_{-0.38}$	$3.36^{+0.45}_{-0.48}$
$Norm_{apec}(cm^{-5})$	-	$0.20^{+0.07}_{-0.05}$	-
$Norm_{vnei}(10^{-2}\,cm^{-5})$	$3.20^{+0.47}_{-0.43}$	$0.69^{+0.08}_{-0.08}$	$4.63^{+0.70}_{-0.70}$
$red.\chi^2/d.o.f.$	1.24/993	1.14/1040	1.54/547

Table 5.5: List of source models and their best fit free parameter values with errors (90% confidence intervals) for the three SNRs. The gaussian has a line at $E \sim 1.23$ keV. All the elemental abundances are given in solar units.

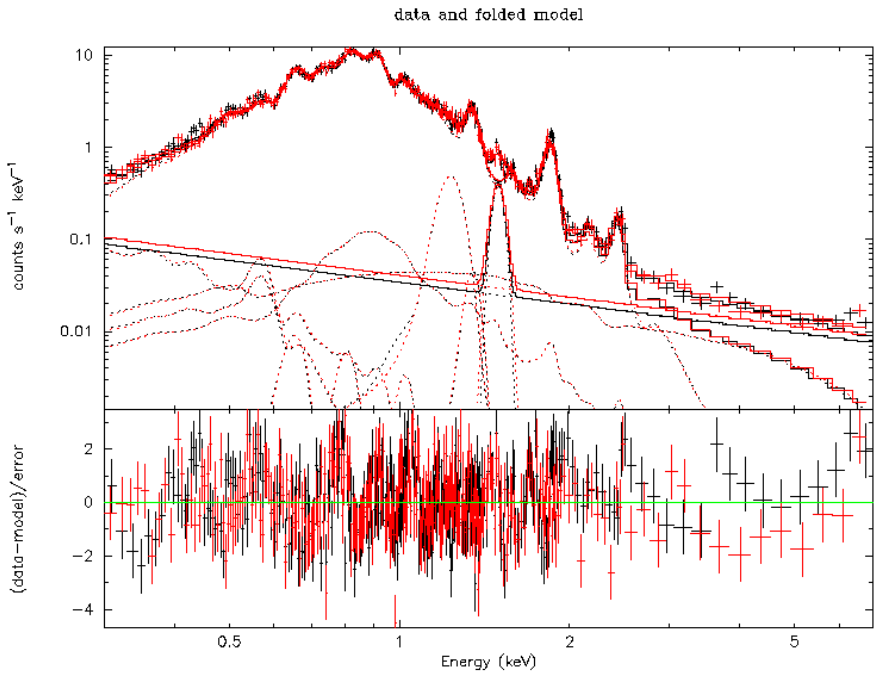

Figure 5.15: Epic spectra of MOS1 and MOS2 data taken from the source region of the SNR G306.3 -0.9 and its best fit model. The solid lines show the main source components (VNEI + GAUS). the delta-χ^2 for the fit is shown in the lower panel.

5.5 Size Estimations

In this section we try to calculate the sizes of the three SNRs. Determining the size of a SNR is an important step in determining the age to understand the stellar evolution timelines. It is useful in calculating the explosion energy and its environmental interaction. The expansion rate of a supernova depends on the surrounding gas density, nearby molecular clouds and magnetic fields. For example, an asymmetric or unusually small SNR usually suggests dense surroundings. The size can be determined using the angular radius of the source, obtained from the selected source region in fig.5.6 using `DS9`, and the distance to the SNRs. SNR G272.2 -3.2 has an uncertain distance. Greiner et al. (1994a) obtained a value of $1.8^{+1.4}_{-0.8}$ kpc by analyzing interstellar absorption, whereas statistical analysis of Harrus et al. (2001) put the value at 2 kpc with an upper limit at 10 kpc. They adopted an intermediate value of 5 kpc. The SNR G306.3 -0.9 on the other hand has a commonly adopted distance of $\sim$ 20 kpc (Sawada et al. (2019)). The SNR G299.2 -2.9 is at a distance of around 5 kpc (Busser et al. (1996)). The distances used in the calculations are shown in the table.5.6. We can confirm the choice of the distances by comparing it to the values of Hydrogen column density (N_H) obtained in the spectral analysis (table.5.6). The relation between them comes from how X-rays are absorbed by the interstellar material along the line of sight. For objects lying in the galactic disk (Zhu et al. (2017); Güver and Özel (2009)), distance to the SNR (D, in kpc) and N_H are related as,

$$N_H \sim (1-2) \times 10^{21} cm^{-2} kpc^{-1} \tag{5.1}$$

assuming average Galactic gas density. The N_H values obtained for the three

sources in the spectral analyses seem to agree with this relation (5.1). The radius of the SNRs is then calculated using the formula (eq.5.2) stated below.

$$r = D.tan(\theta) \tag{5.2}$$

Here r and D are the radius of the SNR and the distance to the SNR in parsec(pc). θ is the angular radius in radians. We approximate $tan(\theta) \sim \theta$ since the angular widths are very small. We finally use the following equation:

$$r(pc) = D(kpc) \times \theta(arcmin) \times 0.291 \tag{5.3}$$

Source	$D\,(kpc)$	$\theta(')$	$r\,(pc)$	$d\,(pc)$
G272.2 -3.2	~ 5	8.22	11.96	23.92
G306.3 -0.9	~ 20	2.09	12.16	24.32
G299.2 -2.9	~ 5	5.55, 4.75	7.47	14.94

Table 5.6: Size measures of the SNRs. The table shows the calculated diameter(d) and radius(r) in parsecs with the distance to the SNRs(D) in kpc and angular radius (θ in arcmins). The anglular radius for the eliptical SNR G299.2 -2.9 is given by the radius of semi-major, semi-minor axes and the r/d is the effective r/d.

Chapter 6

Discussion

6.1 SNR G272.2 -3.2

The Galactic supernova remnant G272.2 -3.2 was first discovered in X-rays by the ROSAT All-sky survey (Greiner et al. (1994b)). It is a young, nearly circular remnant with a centrally brightened morphology in X-rays (fig.5.7). Greiner et al. (1994b) suggests the origin of this central X-ray emission to be the reverse-shocked ejecta from the supernova explosion or cloud evaporation inside the remnant. Spectral Our spectral analysis applies a Variable Non-Equilibrium Ionization (VNEI) plasma model which gives us a high plasma temperature of kT$\sim$0.61 keV. This is in accordance with the values found by Kamitsukasa et al. (2016) i.e $\sim 0.6 - 3.0$ keV obtained from suzaku observations. X-ray analysis by McEntaffer et al. (2013) using Chandra data shows plasma temperatures in the range kT $\sim$ $0.69\,to\,1.5$ keV. They fit the spectrum with a VNEI and VAPEC model at higher and lower energies respectively. This study also gives evidence for a shell-morphology of the SNR which is now a widely accepted result as shown in other recent studies (Sánchez-Ayaso et al. (2013)). Though the centrally brightened and non-shell type morphology in our study suggests that the SNR is a 'thermal-composite' SNR as agreed upon by Harrus et al. (2001). Table.5.5 shows an hydrogen column density of $\sim 1.31 \times 10^{22}\,cm^{-2}$ and an ionization timescale of $\sim 5.85 \times 10^{10} cm^{-3}$s which suggests that the SNR has not reached ionization equilibrium yet. These values are consistent with Sánchez-Ayaso et al. (2013) for the spectral analysis of the regions taken in the center of the SNR. The age of this SNR is not very well constrained. Calculations using the ionization timescales suugests the age of the SNR to be ranging from $\sim$ 4300 yr (Sezer and Gök (2012)) to $\sim$ 8700 yr (McEntaffer et al. (2013)). Multiwavelength analyses and Chandra data predicts an age of $\sim$ 11000 yr (McEntaffer et al. (2013)). The abundances of oxygen are subsolar whereas S, Si have higher abundances. The best fit model in our study does not show any Fe abundances as opposed to other studies mentioned in this section which show higher abundances of the Fe-group elements and conclude the SNR to be type Ia (Sezer and Gök (2012)). This mentioned Suzaku study also reports lesser abundance of Fe relative to the other Fe-group elements and reasons that this may be due to the Fe-rich core not yet being completely shocked like in the case of SN 1006 (Yamaguchi et al. (2008)).

6.2 SNR G306.3 -0.9

This Galactic supernova remnant was first discovered by the *Swift* Galactic Plane Survey in 2011 (Miller et al. (2011)). The X-ray reveals an asymmetric circular morphology with a semi-circularly brightened structure in the south (fig.5.8). This is consistent with the morphology obtained from X-ray and *Spitzer* radio data by Combi et al. (2016). Older literature suggests the age of the SNR to $\sim$ 2.5 kyr assuming a distance of 8 kpc (Reynolds et al. (2013)). Recent studies of comparison of X-ray absorption with the H I distribution suggests a larger distance of $\sim$ 20 kpc (sect.5.5) and suggests the SNR to be $\sim$ 6 kyr old. The data is modeled using two absorbed thermal plasma components: APEC and VNEI, in equilibrium ionization with temperature kT$\sim$ 0.21 keV and non-equilibrium ionization with temperature kT$\sim$ 1.03 keV, respectively. Recent XMM-Newton and Chandra study done by Weng et al. (2022) initially using the same model with tempertures kT $\sim 0.2\, and\, 1$ keV for the hot and cold component respectively. They then used a triple component model (APEC + VNEI + VNEI_{Fe}) to also include a Fe-rich gas with temperatures kT_{cold}, kT_{hot}, kT_{Fe} obtained as $\sim$ 0.21, $\sim$ 0.72 and $\sim$ 3.06 keV, respectively. They also include the Fe-L emission line at $\sim$ 1.22 keV. The spectral model in our study (table.5.5) shows increasing abundances of the Fe-group elements with an especially high abundance of calcium (Ca). Similar results were obtained by Sezer et al. (2017), Sawada et al. (2019) and Weng et al. (2022). Previous studies of the Fe-Kα emission lines by Combi et al. (2016), Sezer et al. (2017) and Sawada et al. (2019) concluded Type Ia origins of the SNR. But the high Ca-abundances obtained in our study (similarly by Weng et al. (2022)) suggest the SNR to be Ca-rich transient making it the first identified Galactic Ca-rich transient SNR. An explanation for the excess abundance of Ca can be due to the burning of He-rich matter which can be through two possible necleosynthesis models: one, the accreted White Dwarf (WD) He-shell detonation (Waldman et al. (2011)) and second,the merger of a He-rich WD and a neutron star (Margalit and Metzger (2016)). Of these, Weng et al. (2022) reasons for a preferred He-shell detonation model.

6.3 SNR G299.2 -2.9

The Galactic SNR G299.2 -2.9 shows a clear asymmetric shell-type morphology (fig.5.9). The imaging also shows faint emission extending beyond the shell specially in the west. We also see knot structures overlapping the shell in the north-east region. Results from Chandra observations by Park et al. (2007) show similar results. It attributes the faint emissions as a consequence of the SNR expanding in an inhomogeneous interstellar medium (ISM) with a density gradient. The high density ISM region slows the shock down, producing bright limb-brightening emission like in the main shell. In the lower density ISM, on the other hand, the shock can traverse farther and faster producing weaker emissions. Post et al. (2014) used a deeper data and a wider field of view of the ACIS-I array to study this asymmetry. The spectral analysis of different regions of this SNR suggested an uneven distribution of metal abundances. The Fe/Si ratio was higher in the northern ejecta than the southern part. Hence, it also brings into picture the possibility of an uneven supernova explosion. Our X-ray data was modeled with a

VNEI component with temperature kT$\sim$ 0.45 keV and an ionization timescale of $\sim 3.24 \times 10^{10}\, cm^{-3}$s. The X-ray spectral fit shows very prominent lines of heavy elements (fig.5.15) like Si, S, Ar, Fe and Ni (table.5.5). Ni shows a notably high abundance and could not be constrained with the Fe abundance, hence, it had to kept free. Stable Ni is usually produced in high-density burning regions. The high Ni/Fe implies that the reverse shock has propagated deep into the remnant and that the core material is now emitting in X-rays which is very characteristic of a Type Ia SNR. A region-wise spectral analysis could help us know if the Ni is localized or wide-spread. This is important because localized Ni may signify an asymmetric explosion (Chamulak et al. (2012)) or the presence of clumpy ejecta. Considering a distance of $\sim$ 5 kpc, Park et al. (2007) calculates the SNR to be $\sim$ 4.5 kyr old.

6.4 Comparisons of the three SNRs

The identifying negative galactic latitudes of the three supernova remnants: G272.2 -3.2 (G272), G306.3 -0.9 (G306) and G299.2 -2.9 (G299 for this section) suggest that they all lie south of the galactic plane. G272 lies the farthest from the plane and at a distance of $\sim 2-5$ kpc from the center of the plane placing it in the thin disk population of the Carina-Sagittarius arm. The G299 is at a distance of $\sim$ 5 kpc as well but closer to the galactic plane than the G272. It lies near the Carina spiral arm which also hosts many massive stars and supernova remnants. Lastly, G306 lies closest to the galactic plane but farthest in distance along the plane placing it in the Perseus arm (Camargo et al. (2015)). This closeness of the G306 to the galactic plane is evident in its comparatively higher N_H values as the disk contains more gas and dust. The analyses of the three SNRs suggest that G306 has a higher ionization timescale value ($\times 10^{11}\, cm^{-3}$s) compared to the other two ($\times 10^{10}\, cm^{-3}$s). Its cool component is modeled using an extra collisional ionization equilibrium (CIE-APEC) component unlike the other two SNRs. G272 and G306 have a similar circular shape and nearly same sizes (table.5.6), though the G272 appears brighter due to its closeness to us. The G299 shows different morphology than the others such that its not circular but has a more elliptical shape with a shell structure as discussed in the previous section. The spatial diversity of the three SNRs make them useful for studying how the ISM and Galactic environments influence SNR evolution.

Chapter 7

Conclusion

The study presents a detailed X-ray spectral analysis of the three Galactic Supernova Remnants (SNRs): G272.2 -3.2, G306.3 -0.9 and G299.2 -2.9. The spectral properties of these SNRs were investigated in an attempt to constrain their plasma conditions, chemical compositions and evolutionary states. The spectral modeling suggests that the X-ray emission of all the three remnants is dominated by thermal plasma emissions, though their plasma conditions differ significantly amongst them. The best fit models suggest plasma temperatures of $\sim$ 0.61 keV for SNR G272.2 -3.2, $\sim$ 0.45 keV for SNR G299.2 -2.9 and $\sim$ 0.21 keV and $\sim$ 1.03 keV for the cold and hot component of SNR G306.3 -0.9. The ionization timescales suggest that G306.3 -0.9 ($\tau \sim (\times 10^{11})\, cm^{-3}$s) is closer to ionization equilibrium than G272.2 -3.2 and G299.2 -2.9 with $\tau \sim (\times 10^{10})\, cm^{-3}$s. These variations of ionization timescales are within the range of the values obtained for Galactic SNRs and provide an insight into their age, explosion energy and the density of the ambient medium. Elemental abundances derived from the spectral fits reveal clear evidence of metal enrichment in the in the emitted plasma. Except for SNR G272.2 -3.2, the other two SNRs show enhanced abundances of heavy group elements like Si, S, Ar, Ca and Fe supporting the notion that the observed emission is dominated by the shocked-ejecta rather than the swept up interstellar material. The SNR G306.3 -0.9 shows very high abundance of Ca which along with other characteristics classify it as a Ca-rich transient. The elemental abundances and a shell-type X-ray morphology of the SNR G299.2 -2.9 suggest a type Ia SN. The detection of the Fe-L line emission at E$\sim$ 1.23 keV (Smith et al. (2001)) in the X-ray spectra of the SNRs supports the presence of line emissions from highly ionized elements in the hot plasma. Such line features are typical in SNR spectra and provide further diagnostics for the plasma temperatures, ionization states and elemental compositions. The reduced chi-square values obtained from the spectral fitting for all the sources indicates that the models used in the analysis provides a statistically reasonable representation of the observed spectra. The normalization parameters can be further used to calculate the emission measures of the SNRs.

Overall, the study highlights the diversity of the physical and dynamic conditions present in the Galactic supernova remnants. The results showing different temperatures, elemental abundances and ionization states suggest differences in their evolutionary stages and interactions with the surrounding interstellar medium. These findings contribute to the deeper understanding of the physical processes that govern the evolution of SNRs and their role in enriching the sur-

rounding interstellar medium and in turn affecting the chemistry of an galaxy in which they lie.

Future missions (for example: the NewAthena mission) that incorporate higher resolution X-ray spectroscopy, multiwavelength observations and spatially resolved spectral analysis will provide better insights into the structure and evolution of these supernova remnants. These observations would help us better constrain the progenitor types, environmental conditions and explosion mechanisms that shape the observed SNR properties.

Bibliography

Arnaud, K. A. (1996). XSPEC: The First Ten Years. In Jacoby, G. H. and Barnes, J., editors, *Astronomical Data Analysis Software and Systems V*, volume 101 of *Astronomical Society of the Pacific Conference Series*, page 17.

Borkowski, K. J., Reynolds, S. P., Hwang, U., Green, D. A., Petre, R., Krishnamurthy, K., and Willett, R. (2013). Supernova Ejecta in the Youngest Galactic Supernova Remnant G1.9+0.3. , 771(1):L9.

Busser, J.-U., Egger, R., and Aschenbach, B. (1996). G299.2-2.9: a new galactic supernova remnant. , 310:L1–L4.

Camargo, D., Bonatto, C., and Bica, E. (2015). Tracing the galactic spiral structure with embedded clusters. *Monthly Notices of the Royal Astronomical Society*, 450(4):4150–4160.

Chamulak, D. A., Meakin, C. A., Seitenzahl, I. R., and Truran, J. W. (2012). Asymmetry and the Nucleosynthetic Signature of Nearly Edge-lit Detonation in White Dwarf Cores. , 744(1):27.

Chen, L.-W., Fabian, A. C., and Gendreau, K. C. (1997). ASCA and ROSAT observations of the QSF3 field: the X-ray background in the 0.1-7 keV band. , 285(3):449–471.

Chevalier, R. A. (1982). Self-similar solutions for the interaction of stellar ejecta with an external medium. , 258:790–797.

Combi, J. A., García, F., Suárez, A. E., Luque-Escamilla, P. L., Paron, S., and Miceli, M. (2016). Detailed study of SNR G306.3-0.9 using XMM-Newton and Chandra observations. , 592:A125.

de Chambure, D., Lainé, R., van Katwijk, K., and Kletzkine, P. (1999). XMM's X-ray telescopes. *ESA Bulletin*, 100:30–42.

Draine, B. T. (2011). *Physics of the Interstellar and Intergalactic Medium*. Princeton University Press, Princeton, NJ.

Ferrand, G. and Safi-Harb, S. (2012). A census of high-energy observations of Galactic supernova remnants. *Advances in Space Research*, 49(9):1313–1319.

Field, G. B., Goldsmith, D. W., and Habing, H. J. (1969). Cosmic-Ray Heating of the Interstellar Gas. , 155:L149.

Filippenko, A. V. (1997). Optical Spectra of Supernovae. , 35:309–355.

Green, D. A. (2025). An updated catalogue of 310 Galactic supernova remnants and their statistical properties. *Journal of Astrophysics and Astronomy*, 46(1):14.

Greiner, J., Egger, R., and Aschenbach, B. (1994a). G272.2-3.2: a centrally filled and possibly young SNR discovered by ROSAT. , 286:L35–L38.

Greiner, J., Egger, R., and Aschenbach, B. (1994b). G272.2-3.2: a centrally filled and possibly young SNR discovered by ROSAT. , 286:L35–L38.

Güver, T. and Özel, F. (2009). The relation between optical extinction and hydrogen column density in the Galaxy. , 400(4):2050–2053.

Harrus, I. M., Slane, P. O., Smith, R. K., and Hughes, J. P. (2001). A New ASCA and ROSAT Study of the Supernova Remnant G272.2-3.2. , 552(2):614–623.

Heintz, R. (2019). Back illuminated vs. front illuminated ccd-based imaging sensors and how it impacts raman spectra. White Paper WP53197, Thermo Fisher Scientific.

Helder, E. A., Vink, J., Bykov, A. M., Ohira, Y., Raymond, J. C., and Terrier, R. (2012). Observational Signatures of Particle Acceleration in Supernova Remnants. , 173(1-4):369–431.

HI4PI Collaboration, Ben Bekhti, N., Flöer, L., Keller, R., Kerp, J., Lenz, D., Winkel, B., Bailin, J., Calabretta, M. R., Dedes, L., Ford, H. A., Gibson, B. K., Haud, U., Janowiecki, S., Kalberla, P. M. W., Lockman, F. J., McClure-Griffiths, N. M., Murphy, T., Nakanishi, H., Pisano, D. J., and Staveley-Smith, L. (2016). HI4PI: A full-sky H I survey based on EBHIS and GASS. , 594:A116.

Jagoda, N., Austin, G. K., Mickiewicz, S., and Goddard, R. H. (1972). The uhuru x-ray instrument. *IEEE Transactions on Nuclear Science*, 19:579–591.

Jansen, F., Lumb, D., Altieri, B., Clavel, J., Ehle, M., Erd, C., Gabriel, C., Guainazzi, M., Gondoin, P., Much, R., Munoz, R., Santos, M., Schartel, N., Texier, D., and Vacanti, G. (2001). XMM-Newton observatory. I. The spacecraft and operations. , 365:L1–L6.

Kalberla, P. M. W. and Kerp, J. (2009). The H I Distribution of the Milky Way. *Annual Review of Astronomy and Astrophysics*, 47:27–61.

Kamitsukasa, F., Koyama, K., Nakajima, H., Hayashida, K., Mori, K., Katsuda, S., Uchida, H., and Tsunemi, H. (2016). Suzaku study on the ejecta of the supernova remnant G272.2-3.2. , 68:S7.

Khokhlov, A. M. (1991). Delayed detonation model for type IA supernovae. , 245(1):114–128.

Klessen, R. S. and Glover, S. C. O. (2016). *Physical Processes in the Interstellar Medium*, volume 43 of *Saas-Fee Advanced Course*. Springer International Publishing.

Kuntz, K. D. and Snowden, S. L. (2000). Deconstructing the Spectrum of the Soft X-Ray Background. , 543(1):195–215.

Kuntz, K. D. and Snowden, S. L. (2008). The EPIC-MOS particle-induced background spectra. , 478(2):575–596.

Leahy, D. A., Ranasinghe, S., and Gelowitz, M. (2020). Evolutionary models for 43 galactic supernova remnants with distances and x-ray spectra. *The Astrophysical Journal Supplement Series*, 248(1):16.

Manconi, S., Woo, J., Shang, R.-Y., Krivonos, R., Tang, C., Di Mauro, M., Donato, F., Mori, K., and Hailey, C. J. (2024). Geminga's pulsar halo: An X-ray view. , 689:A326.

Margalit, B. and Metzger, B. D. (2016). Time-dependent models of accretion discs with nuclear burning following the tidal disruption of a white dwarf by a neutron star. *Monthly Notices of the Royal Astronomical Society*, 461(2):1154–1176.

McEntaffer, R. L., Grieves, N., and Brantseg, T. (2013). X-ray Emission from the Galactic Supernova Remnant G272.2-3.2. *arXiv e-prints*, page arXiv:1301.0674.

McEntaffer, R. L., Grieves, N., DeRoo, C., and Brantseg, T. (2013). A new x-ray view of the supernova remnant g272.23.2 and its environment. *The Astrophysical Journal*, 774(2):120.

McKee, C. F. and Ostriker, J. P. (1977). A theory of the interstellar medium: three components regulated by supernova explosions in an inhomogeneous substrate. , 218:148–169.

McLaughlin, B., editor (2013). *McGraw-Hill Science and Technology Yearbook 2013*. McGraw-Hill Education, New York.

Miller, J. M., Reynolds, M. R., Maitra, D., Gultekin, K., Gehrels, N., Kennea, J., Siegel, M., Gelbord, J., and Kuin, P. (2011). Discovery of a New Supernova Remnant in the Swift Galactic Plane Survey. *The Astronomer's Telegram*, 3415:1.

Minkowski, R. (1941). Spectra of Supernovae. , 53(314):224.

Okon, H., Uchida, H., Tanaka, T., Matsumura, H., and Tsuru, T. G. (2018). The origin of recombining plasma and the detection of the Fe-K line in the supernova remnant W 28. , 70(3):35.

Park, S., Slane, P. O., Hughes, J. P., Mori, K., Burrows, D. N., and Garmire, G. P. (2007). Chandra X-Ray Study of Galactic Supernova Remnant G299.2-2.9. , 665(2):1173–1181.

Post, S., Park, S., Badenes, C., Burrows, D. N., Hughes, J. P., Lee, J.-J., Mori, K., and Slane, P. O. (2014). Asymmetry in the observed metal-rich ejecta of the galactic type ia supernova remnant g299.22.9. *The Astrophysical Journal Letters*, 792(1):L20.

Ranasinghe, S. and Leahy, D. (2022). Distances, Radial Distribution, and Total Number of Galactic Supernova Remnants. , 940(1):63.

Raymond, J. C. (1979). Shock waves in the interstellar medium. , 39:1–63.

Reynolds, M. T., Loi, S. T., Murphy, T., Miller, J. M., Maitra, D., Gültekin, K., Gehrels, N., Kennea, J. A., Siegel, M. H., Gelbord, J., Kuin, P., Moss, V., Reeves, S., Robbins, W. J., Gaensler, B. M., Reis, R. C., and Petre, R. (2013). G306.3-0.9: A Newly Discovered Young Galactic Supernova Remnant. , 766(2):112.

Sánchez-Ayaso, E., Combi, J. A., Bocchino, F., Albacete-Colombo, J. F., López-Santiago, J., Martí, J., and Castro, E. (2013). XMM-Newton and Chandra observations of G272.2-3.2. Evidence of stellar ejecta in the central region. , 552:A52.

Sato, T., Koyama, K., Lee, S.-H., and Takahashi, T. (2016). Suzaku spectra of a Type-II supernova remnant, Kes 79. , 68:S8.

Sawada, M., Tachibana, K., Uchida, H., Ito, Y., Matsumura, H., Bamba, A., Tsuru, T. G., and Tanaka, T. (2019). Ionization age of iron ejecta in the Galactic Type Ia supernova remnant G306.3-0.9. , 71(3):61.

Sedov, L. I. (1959). *Similarity and Dimensional Methods in Mechanics*. Academic Press, New York.

Sezer, A., Ergin, T., and Yamazaki, R. (2017). Suzaku analysis of the supernova remnant G306.3-0.9 and the gamma-ray view of its neighbourhood. , 466(3):3434–3441.

Sezer, A. and Gök, F. (2012). Suzaku study of the centrally brightened supernova remnant G272.2-3.2. , 421(4):3538–3542.

Smith, R. K., Brickhouse, N. S., Liedahl, D. A., and Raymond, J. C. (2001). Collisional Plasma Models with APEC/APED: Emission-Line Diagnostics of Hydrogen-like and Helium-like Ions. , 556(2):L91–L95.

Snowden, S. L. and Kuntz, K. D. (2023). *Cookbook for Analysis Procedures for XMM-Newton EPIC Observations of Extended Objects and the Diffuse Background*. NASA/GSFC. Updated for SAS Version 21.0.

Snowden, S. L., Mushotzky, R. F., Kuntz, K. D., and Davis, D. S. (2008). A catalog of galaxy clusters observed by XMM-Newton. , 478(2):615–658.

Strüder, L., Briel, U., Dennerl, K., Hartmann, R., Kendziorra, E., Meidinger, N., Pfeffermann, E., Reppin, C., Aschenbach, B., Bornemann, W., Bräuninger, H., Burkert, W., Elender, M., Freyberg, M., Haberl, F., Hartner, G., Heuschmann, F., Hippmann, H., Kastelic, E., Kemmer, S., Kettenring, G., Kink, W., Krause, N., Müller, S., Oppitz, A., Pietsch, W., Popp, M., Predehl, P., Read, A., Stephan, K. H., Stötter, D., Trümper, J., Holl, P., Kemmer, J., Soltau, H., Stötter, R., Weber, U., Weichert, U., von Zanthier, C., Carathanassis, D., Lutz, G., Richter, R. H., Solc, P., Böttcher, H., Kuster, M., Staubert, R., Abbey, A.,

Holland, A., Turner, M., Balasini, M., Bignami, G. F., La Palombara, N., Villa, G., Buttler, W., Gianini, F., Lainé, R., Lumb, D., and Dhez, P. (2001). The European Photon Imaging Camera on XMM-Newton: The pn-CCD camera. , 365:L18–L26.

Taylor, G. I. (1950). The formation of a blast wave by a very intense explosion. i. theoretical discussion. *Proceedings of the Royal Society of London. Series A, Mathematical and Physical Sciences*, 201(1065):159–174.

Tracz, P. (2022). *RF LINAC Design Modelling for Optimization of Beam Parameters for ICS Gamma-Ray Source System*. PhD thesis, University Politehnica of Bucharest.

Turner, M. J. L., Abbey, A., Arnaud, M., Balasini, M., Barbera, M., Belsole, E., Bennie, P. J., Bernard, J. P., Bignami, G. F., Boer, M., Briel, U., Butler, I., Cara, C., Chabaud, C., Cole, R., Collura, A., Conte, M., Cros, A., Denby, M., Dhez, P., Di Coco, G., Dowson, J., Ferrando, P., Ghizzardi, S., Gianotti, F., Goodall, C. V., Gretton, L., Griffiths, R. G., Hainaut, O., Hochedez, J. F., Holland, A. D., Jourdain, E., Kendziorra, E., Lagostina, A., Laine, R., La Palombara, N., Lortholary, M., Lumb, D., Marty, P., Molendi, S., Pigot, C., Poindron, E., Pounds, K. A., Reeves, J. N., Reppin, C., Rothenflug, R., Salvetat, P., Sauvageot, J. L., Schmitt, D., Sembay, S., Short, A. D. T., Spragg, J., Stephen, J., Strüder, L., Tiengo, A., Trifoglio, M., Trümper, J., Vercellone, S., Vigroux, L., Villa, G., Ward, M. J., Whitehead, S., and Zonca, E. (2001). The European Photon Imaging Camera on XMM-Newton: The MOS cameras. , 365:L27–L35.

Villa, G. E., Barbera, M., Collura, A., La Palombara, N., Musso, C., Serio, S., Stillwell, R., Tognon, P., and Turner, D. C. (1998). The optical/UV filters for the EPIC experiment. *IEEE Transactions on Nuclear Science*, 45(3):921–926.

Vink, J. (2012). Supernova remnants: the X-ray perspective. , 20:49.

Waldman, R., Sauer, D., Livne, E., Perets, H., Glasner, A., Mazzali, P., Truran, J. W., and Gal-Yam, A. (2011). Helium shell detonations on low-mass white dwarfs as a possible explanation for sn 2005e. *The Astrophysical Journal*, 738(1):21.

Weng, J., Zhou, P., Chen, Y., Leung, S.-C., Toonen, S., Perets, H. B., Nomoto, K., Zenati, Y., and Vink, J. (2022). Spatially Resolved X-Ray Study of Supernova Remnant G306.3-0.9 with Unusually High Calcium Abundance. , 924(2):119.

Wilms, J., Allen, A., and McCray, R. (2000). On the Absorption of X-Rays in the Interstellar Medium. , 542(2):914–924.

Winkler, F. (2013). Sn 1006 supernova remnant [photograph]. https://www.nasa.gov/universe/supernova-remnant-sn-1006/. NASA/CXC/Middlebury College.

Wolter, H. (1952a). Spiegelsysteme streifenden einfalls als abbildende optiken für röntgenstrahlen. *Annalen der Physik*, 10(1-2):94–114.

Wolter, H. (1952b). Spiegelsysteme streifenden einfalls als abbildende optiken für röntgenstrahlen. ii. *Annalen der Physik*, 10(5-6):286–295.

Woltjer, L. (1972). Supernova Remnants. , 10:129.

XMM-Newton SOC (2025). *XMM-Newton Users Handbook*. European Space Agency (ESA), issue 2.23 edition. https://xmm-tools.cosmos.esa.int/external/xmm_user_support/documentation/uhb/overview.html.

Yamaguchi, H., Badenes, C., Petre, R., Nakano, T., Castro, D., Enoto, T., Hiraga, J. S., Hughes, J. P., Maeda, Y., Nobukawa, M., Safi-Harb, S., Slane, P. O., Smith, R. K., and Uchida, H. (2014). Discriminating the progenitor type of supernova remnants with iron k-shell emission. *The Astrophysical Journal*, 785(2):L27.

Yamaguchi, H., Koyama, K., Katsuda, S., Nakajima, H., Hughes, J. P., Bamba, A., Hiraga, J. S., Mori, K., Ozaki, M., and Tsuru, T. G. (2008). X-Ray Spectroscopy of SN 1006 with Suzaku. , 60:S141.

Zhu, H., Tian, W., Li, A., and Zhang, M. (2017). The gas-to-extinction ratio and the gas distribution in the Galaxy. , 471(3):3494–3528.

Acknowledgment

I would like to extend my gratitude to all the members of the Dr.Karl Remeis Observatory, Bamberg who have always helped me in successfully accomplishing my research. I would like to especially thank Prof. Dr. Manami Sasaki for her constant guidance and patience and for providing me the opportunity to carry out this research under her supervision. I am also thankful to Friedrich Alexander University (FAU) for imparting all the knowledge that I acquired through its offered courses that helped me better understand the concepts involved in this research. Lastly, I am very grateful for my family and friends for their unwavering support and motivation that has helped me navigate through this whole journey.

Thank You

Declaration

I hereby declare that this thesis has been written by me independently. All the data has been obtained from the XMM-Newton Science Archive (XSA). The sources of information used to complete the thesis have been cited in the end.

Place, Date

Signature